Predictions of a galactic outflow model for spectral mapping observations

Bachelor thesis

Anna Lena Schaible

Supervised by

Professor Lutz Wisotzki
Leibniz Institute for Astrophysics Potsdam and
University of Potsdam

and

Professor Jörg Main
Institute for Theoretical Physics I
University of Stuttgart

April 9, 2021

Contents

List of Figures

Zusammenfassung

Einen großen Einflussfaktor für viele Aspekte und Prozesse in der Galaxieentwicklung stellen galaktische Winde (GWs) dar. Diese beeinflussen den Metallverlust in Galaxien, reichern das intergalaktische Medium mit Metallen an, bewegen Gase und verändern das zirkumgalaktische Medium (CGM). Diese Arbeit setzt sich mit GWs und deren Modellierung auseinander. Erstmals wird eine Methode gezeigt, um 3D Datenkuben für sphärische galaktische Ausflüsse zu berechnen um daraus räumlich aufgelöste Spektren vorherzusagen.
Das semi-analytische Linientransfermodell (SALT) für sphärische GWs, abgeleitet von stellaren Winden, wurde von Scarlata und Panagia 2015 eingeführt, bevor das Potential des Messinstruments MUSE bekannt gewesen ist. Seit MUSE ist es möglich im Wellenlängenbereich von 480 nm bis 930 nm bis ins CGM hineinragend Spektren räumlich aufgelöst zu messen und die Emissionskomponente von GWs bis weit in das CGM hineinragend zu detektieren.
Nach Reimplementierung des SALT Modells und Berechnung der P-Cygni Linienprofile für unterschieliche Parameterkonstellationen, wird in dieser Arbeit das SALT Modell übertragen, um numerisch Datenkuben für Galaxien mit Ausflüssen zu berechnen. Die Datenkuben sind 2D räumlich und 1D spektral aufgelöst. Es werden räumlich aufgelösten Spektren für kreisförmige und quadratische Aperturen berechnet, jedoch ist durch das Datenkubus-Modell jede beliebige Aperturgeometrie möglich.
Das mit dem Datenkubus errechnete Spektrum wird räumlich mit einem Moffat Kernel und spektral mit einem Gauss Kernel gefaltet, um mit Messdaten vergleichbar zu sein. Für unterschiedliche zentriere kreisförmige Aperturen wird das Spektrum der Galaxie UDF884 betrachtet, welche einen sphärischen Ausfluss aufweist und von MUSE gemessen wurde.
Zwischen Datenkubus und SALT Modell ergibt sich ein großer Unterschied in der Absorptionskomponente auf. Im SALT Modell wird die absorbierte Energie bei einer bestimmten beobachteten Geschwindigkeit mit der Größe des gesamten Schalenausschnitts skaliert. Jedoch sollte die absorbierte Energie bei einer bestimmten beobachteten Geschwindigkeit mit der Größe der Galaxiescheibe skaliert werden, was im Datenkubus berücksichtigt wird.

Abstract

Galactically scaled outflows are regarded as extremely important for many aspects and processes of galaxy evolution. This thesis focuses on galactic winds and enables the analysis of spatial resolved spherical galactic outflows. For the first time, a method to calculate 3D datacubes for galactic outflows is presented. Spatially resolved spectra of outflows are predicted.
The semi-analytic line transfer outflow model for spherical galactic scaled outflows (SALT), introduced by Scarlata and Panagia in 2015, transfers the formalism of stellar winds to galactic scales. It was published before the potential of instruments like MUSE was understood. Through MUSE, spatially resolved spectra of the CGM regions in the wavelength range of 480nm to 930 nm can be observed. Thereby, galactic outflows can be observed on large scales.
After reimplementing the SALT model and calculating the P-Cygni line profile for different parameter sets, the model is transferred to numerically calculate datacubes of galaxies with an outflow. Our datacubes are 2D spatially resolved and 1D spectrally resolved. A spatially resolved spectral analysis of the outflow is presented for circular and quadratic apertures. Due to this method, every other geometry is possible.
The spectrum gained by the model is spatially convolved by a point spread function with a Moffat kernel and spectrally convolved by a line spread function with a Gauss kernel. After the convolution, the modelled spectrum can be compared to measured data. The spectrum of the galaxy UDF884 with a spherical outflow for different circular centered aperture sizes is presented. By comparing the spectra of the datacube and the SALT model, a significant difference in the absorption component occurs. In the SALT model, the absorbed energy at a certain observed velocity is scaled by the size of the entire shell segment. However, the absorbed energy at a certain observed velocity has to be scaled by the size of the galaxy disk, which is done in the datacube.

Acknowledgements

I thank

... my supervisor Professor Lutz Wisotzki for the opportunity to work on a very interesting and ongoing research topic at the AIP. Thank you for your support, good advice and discussions.

... Professor Jörg Main for being my supervisor at the University of Stuttgart.

... Christian Herenz, who offered me an internship at the ESO in Chile and who connected me with Lutz for a Bachelor topic.

... all members of the galaxy group at the AIP in Potsdam for the amazing weekly galaxy teas, paper discussions, group meetings and presentations. You gave me a close insight in the daily life of an astrophysicist.

... Carolin Liefke and Dominik Elsässer for growing and supporting my interest in astrophysics since the Junior Science Academy.

... my dad, who supported my interest in physics and to whom I owe my curiosity in science.

... my mum for all the support and that you believed in me all the time.

... my brother, who believed in me and supported me all the time. Thank you for all the amazing experiences and many interesting discussions, ideas and suggestions.

... my friends for all helpful advices and for making my university life unique.

... everybody, who supported me and is not listed here.

Without you my Bachelor thesis and Bachelor studies would not have been such an amazing time.

Chapter 1

Introduction

Galactic winds (GWs) play a main part in galaxy evolution and the surrounding medium. "They transport metals out of galaxies, chemically-enriching the inter-galactic medium [(IGM)] and modifying the chemical evolution of galaxies. They affect the surrounding interstellar and circumgalactic media [(CGM)],thereby influencing the growth of galaxies through gas accretion and star-formation" (Heckman and Thompson, 2017).
In this section an overview on galactic winds and outflows is given. In section 1.1 an overview on galactic winds is given, followed by the forbidden transitions in section 1.2. GWs can be observed via lines in the spectrum. These lines are connected to a certain transition in a ion. In observations, there occur lines that are forbidden by selection rules under normal conditions. For modelling galactic winds and their spectral lines, the models of stellar winds can be transferred on galactic scales by assuming a very simple model. The mechanism of stellar winds is well known since the 1970s and many models are existing. This is the reason for introducing stellar winds in detail, especially radiative driven winds in section 1.3. This mechanism of stellar winds is used to model galactic outflows in this thesis. The spectrum of an outflow usually shows a P-Cygni line profile, which is finally introduced in section 1.5.

1.1 Galactic outflows

Gravity and dark energy shape the universe, if we consider large scales. If we look on galactic scales, the observations unravel that this could not be all. We are forced to look in more details of the physics ongoing in "feedback, including star formation and evolution, energetic and chemical recycling in the interstellar medium [(ISM)] and IGM, gas dynamics, and ultimately plasma

magnetohydrodynamics" (Veilleux et al., 2005) to get an understanding of galaxy formation and evolution. The main and dominant part in feedback for galaxy formation and evolution are GWs (Veilleux et al., 2005). GWs play a key role in understanding galaxy evolution. They have impact on the loss of metals in galaxies and enrich the IGM with metals. Also, they remove gas, which would be available for star formation and transform the CGM.
It is observed that significant amounts of gas move outwards in radial direction in galaxies. They reach velocities of hundreds of kilometres per second, even above 1000 km s^{-1}. However, the driving mechanism of these multiphase winds is not clear, from a theoretical point of view. The comparison of theory and observations still has to be completed (Rupke, 2018), (Zhang, 2018).

1.1.1 Historical discovery of galactic winds in M82

GWs were first observed in the galaxy M82, which is visualized in figure 1.1 and is a nearby bright galaxy. M82 is a starburst galaxy, located in a distance of 3.6 Mpc. M82 "is the brightest and best-studied example of a starburst-driven outflow. While the data are therefore the best and most complete, observations of other starburst-driven outflows are qualitatively consistent with those of M 82" (**?**).
By the quote "The filaments on both sides of the plane appear to be expanding from the center along the minor axis with velocities ranging up to about 1000 km/sec. The data suggest that an expulsion of matter took place from the central regions of M82" (Lynds and Sandage, 1963), Lynds and Sandage introduced an interest in looking in more detail on M82, more than forty years ago. (Burbidge et al., 1964) commented that "the activity in M82 is yet another manifestation of the generation of vast fluxes of energy by processes which are not yet properly understood", in the following year. Some researchers discussed GWs, before the observations and discovery of the "explosion" in M82 were made. Thoughts of, whether this explosion is also such a GW, were made. First evidence was delivered by (Oort and Rougoor, 1959) among others. Many researchers spent time on considering how possible it can be that a explosion powers the radial outflow. Parallel to these works, other thoughts were caught up. (Osterbrock, 1960) detected a broad [O II] emission line in some elliptical galaxies. After this detection it was proposed to consider the presence of galactic-scaled winds. The interest in GWs grew and models were developed based on observations (Heckman and Thompson, 2017).

Figure 1.1: M82 is famous of its star formation activity and can be observed brightly at infra-red wavelengths. "Around the galaxy's center, young stars are being born 10 times faster than they are inside our entire Milky Way galaxy. Radiation and energetic particles from these newborn stars carve into the surrounding gas, and the resulting galactic wind compresses enough gas to make millions of more stars" (Garner, 06.10.2017). In M82 galactic outflows were detected the first time.

Since that time, observation instruments improved. "The explosion of optical and near-infrared 3D imaging spectroscopy has revealed the complex, multiphase structure of nearby GWs" (Rupke, 2018). Nowadays, almost the whole electromagnetic spectrum can be observed. It is possible to observe the emission components of the outflow, which are extended in the CGM. It has become clear that GWs are ubiquitous. GWs are a huge area of current research. By using ground-based observations and space-based observations, hight precision data of spatially resolved winds exist. This was first accessible for nearby galaxies at low red-shift and is nowadays also for high-red-shifted galaxies available. There is strong evidence that the "wind-related feedback processes [is the] [...] key to the chemical and thermal evolution of galaxies

and the IGM" (Veilleux et al., 2005).

1.1.2 Energy source of GWs

With the discovery of the outflow in M82 the question arose, what powers the GWs or what is the energy source of the winds. Starburst-driven or AGN-driven (by an active galactic nucleus) feedback or a combination of both seem to explain these winds.

Starburst driven winds

"Galactic winds from star-forming galaxies are crucial to the process of galaxy formation and evolution, regulating star formation, shaping the stellar mass function and the mass-metallicity relation, and enriching the intergalactic medium with metals. " (Zhang, 2018). Starburst driven GWs are driven by the combination of momentum and mechanical energy form supernovae (SN) and stellar winds (Veilleux et al., 2005).
Stellar-driven GWs play a importat role in young starburst regions. They are dominant in low-mass galaxies and in starbursts without AGN activities. The galaxy M82 is an example for starbursts without AGN activities (Zhang, 2018).

Active galactic nucleus (AGN) driven winds

Many galaxies have in their center a black hole (BH) or a supermassive black hole (SMBH). GWs are also powered by the SMBH activities. AGN feedback has an significant impact in massive galaxies and their formation.
AGN driven outflows consist of ionized and molecular gas, which can be produced by interaction of the surrounding material with the radiation from the accretion disk of the SMBH (Meena et al., 2021).
There exist two modes of AGN feedback: The quasar or radiative mode occurs in high-luminosity AGNs, typical in young quasars at high redshift. "Most of the energy is released by radiation from accretion disks around SMBHs, and radiation couples to the gas, transfers momentum to it, and drives it from the host galaxies" (Zhang, 2018). The second mode is the radio or kinetic mode describes low-luminosity AGNs with radio jets as main source, typical are local massive galaxies.
The significance of AGN feedback is still unclear, from the view of an observer. Simulations are very convincing for AGN feedback. Indeed, there are any outflows. However, which significance they have is far from clear.

1.1.3 Role of GWs in the galaxy evolution

GWs play a crucial key role in galaxy evolution. They also provide energy, mass and metal to the ISM and CGM and play a key role in the evolution of them. Thereby, they determine the growth of galaxies.
"Emission lines such as Hα, N II, O II, O III, and absorptions such as Na I D, K I, Mg II have been used to trace morphologies and velocities of warm, cool and cold outflows in galactic winds, including warm ionized, neutral atomic, molecular, and dust outflows" (Zhang, 2018).
The outflowing gas is supplied into the CGM and IGM. In dwarf galaxies and in massive galaxies, GWs heat the gas in the ISM and impede the gas from cooling down and forming stars, on galactic scales. However, if the gas is moving slower than the escape velocity, the wind can fall back to the galaxy. This can create a galactic fountain and can lead to inflows. This enables to establish the gas-recycling process in galaxies (Zhang, 2018).
GWs influence the chemical evolution of galaxies. They transport metals out of the galaxies. These momentum- or energy-driven winds enrich the CGM and the IGM with metals. In our universe, half of the metals are outside of the galaxies (Heckman and Thompson, 2017). In nuclear reactions, heavy elements are created in stars and SN. These heavy elements are polluted into the IGM by GWs. Galaxies loose lots of metals. Massive galaxies keep more of the wind material, because they have a deeper gravitational potential. Lower mass galaxies, like dwarf galaxies, loose more material (Veilleux et al., 2005), (Heckman and Thompson, 2017). The metal loss from galaxies and the mass of the galaxies are anti-correlated (Zhang, 2018).
On galactic scales and on cosmological scales, the galaxy luminosity function is shaped by GWs. "The observed galaxy luminosity function shows a flat low-mass-end slope and sharp exponential cut-off at the high-mass-end [...]. The high-mass-end can be explained by the AGN feedback, while the flat low-mass-end of the galaxy luminosity is believed to be caused by stellar feedback [...]" (Zhang, 2018).
Galactic winds are essential to get an understanding of galaxy evolution. However, the mechanism of galactic winds is far from clear and current research is ongoing at this topic.

1.2 Forbidden transition

GWs can be observed and analysed by spectral lines in the measured spectrum. Each observed transition frequency is connected to a certain ion or atom and a certain transition. In astrophysical observations, emission lines of so

called forbidden transitions often appear. Normally these transitions can not be created in laboratories and are mainly observed in astrophysics. These transitions are not expected to be seen, because they are usually forbidden by a certain selection rule. However, if the approximation associated with that rule is not valid, the transition is possible. Forbidden emission lines are observed in hot and low-density plasmas in astrophysics. Forbidden emission lines are produced in low-density and optical-thin media. Examples are solar corona, the interstellar medium, stellar atmospheres and planetary nebulae. In these areas of low densities of only a few atoms per cubic meter atomic collisions become really unlikely. Usually atoms are de-excited through collisions, before they could de-excite via emitting radiation. For these low particle densities the time between collisions increases so that this intercollisiontime is larger than the time of occupation of the metastable state. Under such circumstances it is almost clear that if a atom is excited in a metastable state, it will decay by emitting a forbidden transition photon (Eidelsberg et al., 1981).
For transitions in quantum-mechanical systems selection rules exist. this means only transitions are allowed by the selection rules. There are several reasons, why a such called "forbidden transition" is allowed[1]:

- The selection rules are derived by approximations. So a forbidden transition can occur, because it only violates the approximate rule. For example there are some selection rules that are only exact, if there is no spin-orbit coupling. If spin-orbit coupling is present some forbidden transitions get allowed.

- The violated selection rule is only valid for dipole radiation. For the selection rule only the interaction between an atom (quantum-mechanical system) and a electromagnetic field, so only the electric dipole, is considered. However, in the occurring transition magnetic dipole radiation or quadrupole radiation could play an important role for this forbidden transition.

- It can also be that the violated selection rule is only valid for a an isolated atom or isolated molecule. So in the selection rule external fields or collisions may not be taken into account.

Allowed transitions are much stronger than forbidden transition. The electric dipole transition (E1) delivers the selection rules for allowed transitions. An electric dipole transition has the following selection rules:

- $\Delta S = 0$ (same spin)

[1] A Dictionary of Physics, Oxford University Press, 2009, ISBN 9780199233991, doi: 10.1093/acref/9780199233991.001.0001

- $\Delta L = 0, \pm 1$ (orbital angular momentum)
- $\Delta J = 0, \pm 1$ (total angular momentum)
- $\Delta m = 0, \pm 1$ (magnetic quantum number, describes the polarisation of the light)
- Parity changes

Higher order transitions like the second order electric transition or the magnetic transition can occur, if the electric dipole transition is "forbidden". Semi-forbidden transitions satisfy all the selection rules. However, they do not satisfy the spin rule and so semi-forbidden transitions are transitions with $\Delta S \neq 0$. Sometimes, they are also called inter-combination of inter-system lines. A semi-forbidden transition is for example the transition between the helium singlet level and the helium triplet level. Semi-forbidden lines can be seen in notation by "]" on the right of the name of the line.
Forbidden lines are noted by "[...]". Types of forbidden lines are:

- **el quadrupole (E2)**: $\Delta J = 0, \pm 1, \pm 2$ and the parity does not change
- **magn. Dipole (M1)**: $\Delta J = 0, \pm 1$ and the parity does not change
- **el. octupole (E3)**: $\Delta J = \pm 2, \pm 3$ and the parity changes
- **magn. quadrupole (M2)**: $\Delta J = \pm 2$ and the parity changes

((Kulkarni, 2020) and (Pasternack, 1940))

1.3 Stellar winds

In this thesis GWs are modelled by transferring a stellar wind model on galactic scales. The mechanism of resonant radiative driven stellar winds is introduced on galactic scales. Before starting working with a model introduced on galactic scales, a short overview on stellar winds is presented.
Gas from the outer atmosphere is ejected into the interstellar medium (ISM). This can be observed and the phenomenon of outflowing gas from stars is called stellar wind. Stellar winds and the theory of different types are well established. There are four main types of stellar winds (Lamers and Levesque, 2017):

- **Line-driven winds** appear in hot stars and are driven by the radiation pressure on ionized atoms. These winds gain velocities of thousands of km/s and can also have a high mass-loss rate.

- **Dust-driven winds** are also driven by radiation power. However, this mechanism works, as the name says, on dust grains.
- **Coronal winds**: Due to the high temperature of the stellar coronae, the wind is driven by the gas pressure.
- **Alfen wave driven winds**: This type of wind occurs in the presence of magnetic fields and is driven by magnetic waves.

Line-driven winds are used to describe the galactic outflows in the used model. Therefore, a detailed look is presented at resonant radiative driven winds.

1.4 Resonant radiative driven winds

To characterize winds of hot stars the principle of radiative driven winds is used. The established models are for hot and not spatial resolved stars.

1.4.1 Momentum and energy transfer by photons

Each type of ion has a specific spectral line. The ion can experience a radiation force. Without the Doppler effect it would not be efficient to drive a stellar wind by radiation. The radiation of the wavelength of the spectral line from the photosphere would be absorbed by the layers around the photosphere. Outer layers would not receive radiation in the wavelength of the spectral line. Due to the movement of the outer parts of the shells, there arises a velocity gradient. The ions moving in the outer areas see the photons from the photosphere redshifted. This enables these outer shells to absorb photons, which could not be absorbed by inner shells. Through this use of the Doppler effect, the radiation acceleration is very efficient for driving these hot stellar winds (Lamers and Cassinelli, 1999).
Momentum and energy are transferred to the gas and atoms via ions absorbing and re-emitting photons. For easier calculations it is assumed that the absorbing and re-emitting ion moves radially outwards with a velocity v_a. Through absorption the momentum of the photon is transferred to the atom. The atom gains a higher momentum of

$$mv'_\mathrm{a} = mv_\mathrm{a} + \frac{h\nu}{c}, \tag{1.1}$$

which increases the velocity by the amount of $\frac{h\nu}{mc}$. After a certain lifetime the atom re-emits a photon. This photon is emitted arbitrarily in all directions.

By defining the angle α as shown in 1.2, the atom has a momentum of

$$mv''_{\mathrm{a}} = mv'_{\mathrm{a}} - \frac{h\nu}{c}\cos(\alpha). \tag{1.2}$$

If we look on a sort of atoms with no doublet structure, the atom can only absorb photons at a certain frequency ν_0 (in the rest frame of the atom). A potential observer somewhere else does not see this frequency ν_0. He observes a shifted frequency of $\nu_0\left(1+\frac{v_{\mathrm{a}}}{c}\right)$, shifted due to the Doppler effect. Including the Doppler effect, the resulting velocity of the atom is described by

$$v''_{\mathrm{a}} = v_{\mathrm{a}} + \frac{h\nu_0}{mc}\left(1+\frac{v_{\mathrm{a}}}{c}\right) - \frac{h\nu_0}{mc}\left(1+\frac{v'_{\mathrm{a}}}{c}\right)\cos(\alpha) \tag{1.3}$$

$$= v_{\mathrm{a}} + \frac{h\nu_0}{mc}\left(1+\frac{v_{\mathrm{a}}}{c}\right)(1-\cos(\alpha)) - \frac{1}{c}\left(\frac{h\nu_0}{mc}\right)^2\left(1+\frac{v_{\mathrm{a}}}{c}\right)\cos(\alpha). \tag{1.4}$$

Let us assume that the velocity of the particle is small compared to the speed of light ($v \ll c$) and that the momentum of the particle is much higher than the momentum of the photon ($h\nu_0 \ll mc$). Therefore, the velocity of the atom has increased by

$$v''_{\mathrm{a}} - v_{\mathrm{a}} = \frac{h\nu_0}{mc}(1-\cos(\alpha)) \tag{1.5}$$

in radial direction. If the photon of the emission process is re-emitted in outward radial direction, the total amount of momentum of the atom does not increase in the complete absorption and re-emission process. If the re-emitted photon is re-emitted backwards in radial direction, the atom gains an additional momentum in the absorption-emission process of twice of the absorption part. The average momentum transferred to the ion can be calculated by

$$\langle \Delta mv \rangle = \frac{h\nu_0}{c}\frac{1}{4\pi}\int_{-\pi/2}^{\pi/2} \mathrm{d}\alpha \int_0^{2\pi} \mathrm{d}\phi(1-\cos(\alpha))\sin(\alpha) \tag{1.6}$$

$$= \frac{h\nu_0}{c}\frac{1}{4\pi}\int_{-\pi/2}^{\pi/2} \mathrm{d}\alpha 2\pi(1-\cos(\alpha))\sin(\alpha) \tag{1.7}$$

$$= \frac{h\nu_0}{c} \tag{1.8}$$

integrating over the sphere. The photons are re-emitted arbitrarily randomly in all directions, so on average the emission transfers no momentum to the atom, only the absorption process transfers a momentum of $\frac{h\nu_0}{c}$. If the photons for the absorption would come from all directions, the transferred

momentum would cancel out. However, the major part of photons origins from the photosphere and is directed in outward radial direction (Lamers and Cassinelli, 1999).

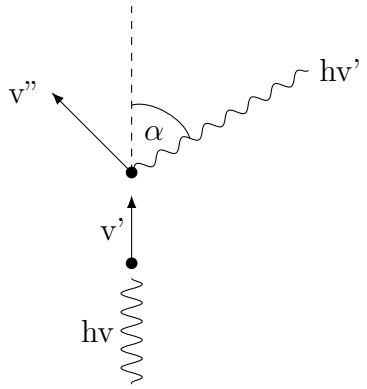

Figure 1.2: The momentum of the photon accelerates the atom in the absorption process in outwards radial direction. In the emission process, the photon is re-emitted in an arbitrary angle and the momenta transferred by the emission process cancels out (Lamers and Cassinelli, 1999).

A example calculation to get an idea of properties: An ion is accelerated by 20 cm/s in one absorption process. They share the momentum to the other wind particles. So, effectively the ion is accelerated in velocity in about $2 \cdot 10^{-3}$ cm/s. Hot stellar winds reach velocities of thousands of km/s and they reach these velocities over a short acceleration zone. Assuming a final velocity of 2000 km/s and a acceleration range of ten solar radii, the ions have to absorb 10^7 photons per second (Lamers and Cassinelli, 1999). This means mainly transitions to levels with a short lifetime contribute to this process.

1.4.2 Momentum and energy transfer by ions

In hot resonant line driven winds of stars, the photons transfer momentum and energy to the ions. This transfer mainly appears at "C, N, O, Ne, Si, P, S and Fe-group elements" (Lamers and Cassinelli, 1999).
The wind material does not only consist of these ions and elements, there are also other particles in the wind. The momentum gained by the ions has to be shared to the other particles to be an outflow of the whole plasma.
This can be achieved due to the electric charge of the ions and the mechanism is called "Coulomb coupling". In a dense environment all particles are in

movement and the ions are slowed down soon. The transfer is done via Coulomb collisions (Puls et al., 2008).

1.5 P-Cygni line profile

P-Cygni profiles are important in astrophysics of outflows. This special line profile appears in stellar winds and in galactic winds. A P-Cygni line profile indicates an outflow and a "P Cygni profiles are [an] [...] example of how line profile shapes are determined by the large-scale flow of material in and around stellar systems" (Robinson, 2007).

1.5.1 Historical discovery of the P-Cygni profile

They are named after the first star were this typical P-Cygni line profile and outflows were discovered. On August 18, 1600, Willem Janszoon Blaeu observed and reported as the first the existence of the new star in the constellation Cygnus. He was a Dutch cartographer and astronomer. He recorded P-Cygni as a supernova (34 Cyg,HR 7763, HD 193237). This object was visible with the naked eye. It remained bright for some years and then the brightness decreased under naked eye visibility. In 1626 and 1655 it returned again to be visible with the naked eye. This variable star has become famous in astrophysics. P-Cygni is a very massive star and one of the brightest and very luminous objects. A historical map of the constellation Cygnus with the star P-Cygni in it is provided in figure 1.3. Such massive stars only last for a few million years. They start in formation and end in a supernovae. P-Cygni is very luminous and blows off its outer layers. So P-Cygni is surrounded by a stellar wind (Israelian and de Groot, 1999), (Snow et al., 1994).
In the spectrum of P-Cygni, there were emission lines from hydrogen, helium and other elements observed. These emission lines were broader than expected by experiments in laboratories or by observations of the sun. In the 1920s it was explained that these broad lines occur due to Doppler shifts, because the material emitting the photons is moving with hundreds of kilometres per second away from the object. In 1897, a strange shape in the emission component was documented. The spectrum showed something like an absorption line in the blueshifted part (Israelian and de Groot, 1999).

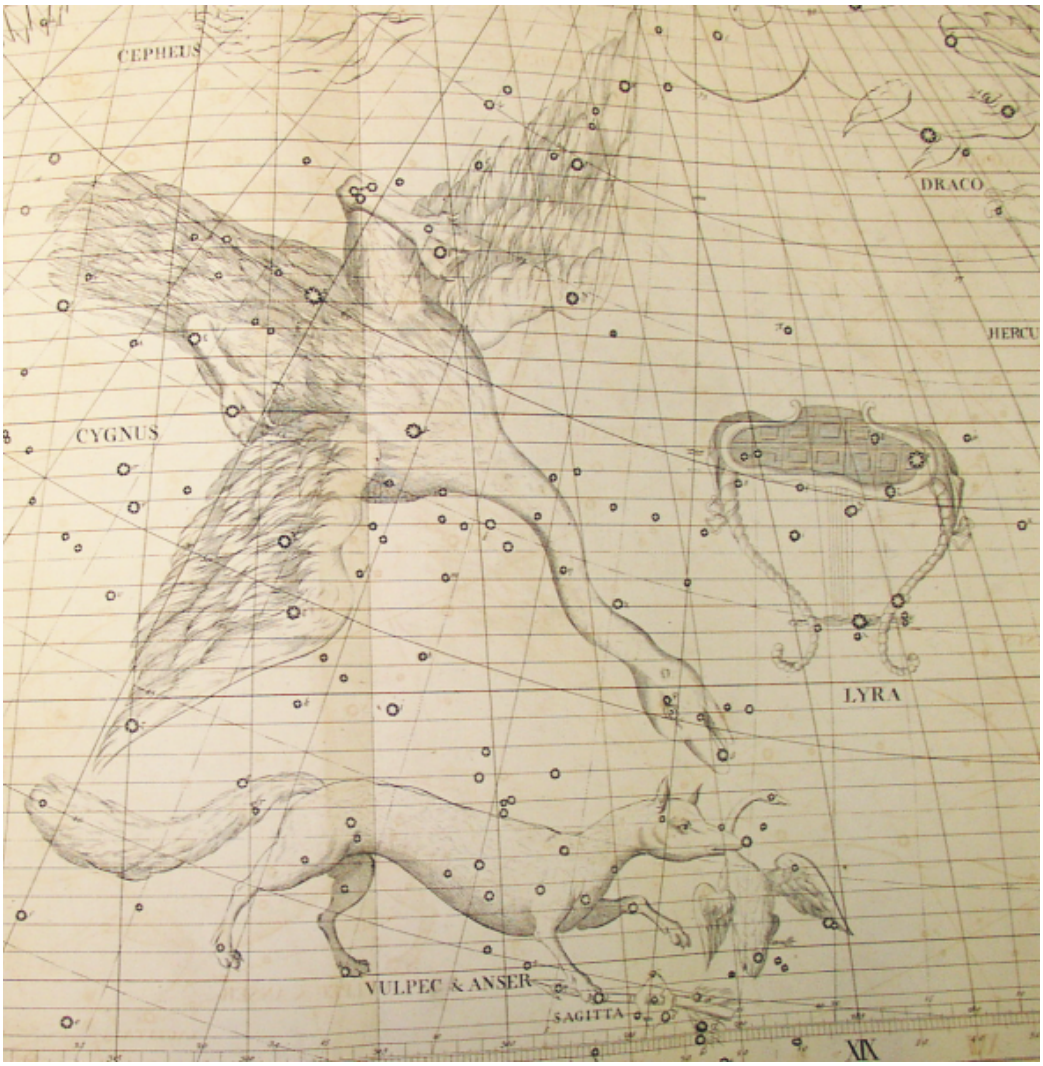

Figure 1.3: "A chart of the Cygnus-Lyra-Vulpecula region from Flamsteed's Atlas Coelestis (from the AAVSO Archives)"[2].

1.5.2 Formation of the P-Cygni profile

The theoretical background of stellar outflow models is well known since the 1970s. If you observe a typical P-Cygni line profile, it is always a good hint for an outflow. P-Cygni line profiles are observed at stellar driven outflows as well as at outflows on galactic scales.
The central effect that creates such a profile is the Doppler effect, which is

[2] https://www.aavso.org/vsots_pcyg

also mentioned in section 1.4. Outside the wind, an observer at rest sees the frequencies of different parts of the wind Doppler shifted.
In the front part, the observer sees an increase in velocity. The outermost ions

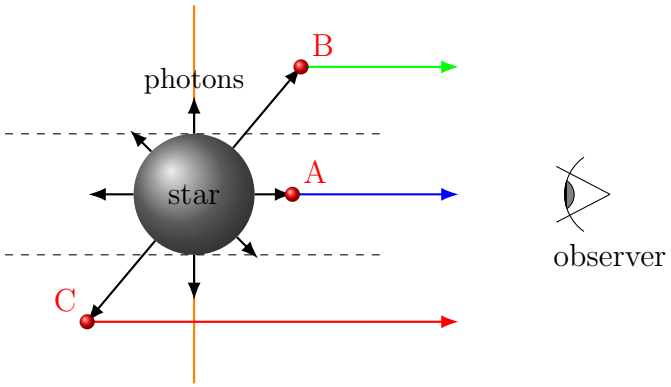

Figure 1.4: In region A, absorption can be observed, which is for an observer blueshifted. The absorption component is observable in front of the continuum source. In region B, in the front part of the shells, only the blueshifted emission component can be seen. In region C, in the backwards part of the shells, the redshifted emission component is created. In total, these areas together create a P-Cygni line profile in the observed spectral line.

have the highest velocity for him. He sees the frequency of these transitions on a higher frequency than the other moving ions would see it. These frequencies are blueshifted due to the Doppler effect for an observer. In the innermost parts, the ions have a low velocity. A potential observer sees the frequencies almost at the same frequency as the co-moving wind particles. In the parts moving backwards, the observer detects a lower frequency than a co-moving wind particle would see. These frequencies are redshifted due to the Doppler effect.
The absorption process can be observed in front of a continuum source, so the velocities are blueshifted compared to the star. The continuum photon excites an electron. Absorption close to the transition line takes place in the inner parts of the wind material. Absorption of photons at higher frequencies takes place in the outer parts of the wind. Absorption takes place in the velocity range of 0 up to $v_{\max}$. In the other ranges of velocity there are no ions, which can absorb these photons and could be seen by an observer.
At the absorption process, an electron gets excited. The excited state has a certain lifetime. After this lifetime, a new photon is re-emitted. The emission process provides additional radiation to the line profile. In the emission, an observer can see the contributions to the line from the forward

and backward parts of the moving wind shells. The absorption process can only be seen in front of the stellar continuum. However, absorption takes place in all areas. The emission can be seen without a continuum, because in this process radiation is emitted and so emission can be detected in the whole envelope. The parts moving towards the observer are bluesifted compared to the systemic line of the ion. Parts moving backwards are redshifted compared to the systemic line of the ion. The emission profile is asymmetric, because in the redshifted parts some areas are occulted by the radiation object [3].
In total, an observer observes the absorption and emission together, which leads to the observation of a P-Cygni profile. This is shown in figure 2.4. This is a typical profile, which is observed, if the object has a wind.
If the material is inflowing and not outflowing, the absorption component is redshifted, which is an inverse P-Cygni line profile[4].

[3]Joachim Puls, Astrophysics Lab A - Winds from Hot Stars, University Observatory Munich, https://www.usm.uni-muenchen.de/people/puls/lessons/hotwindsprakt/stellar_winds.pdf

[4]A Dictionary of Astrophysics, Oxford University Press, 2012, ISBN 9780199609055, doi: 10.1093/acref/9780199609055.001.0001

Chapter 2

SALT model for galactic outflows

The semi-analytical line transfer model (SALT) for spherical galactic outflows introduced by Scarlata and Panagia (Scarlata and Panagia, 2015) describes outflows on galactic scales. They extended the existing outflow model of hot, radiative driven winds, described by (Castor et al., 1975) and (Scuderi et al., 1994) on galactic scales. They are interested in looking on the transition of silicon ions in the stacked spectrum of Lyα emitters at redshift 0.3. In this chapter, the explanation is paraphrased from the first publication of a galactic wind model of Scarlata and Panagia (Scarlata and Panagia, 2015), if not otherwise indicated. With this model, they studied the typical asymmetric resonant absorption and re-emission line profiles from expanding galactic outflows.
In section 2.1 I introduce the outflow model like it is done in (Scarlata and Panagia, 2015) by using a different notation for some variables. In section 2.2 I summarize all assumptions that lead to the model and look in more detail on the Sobolev approximation in section 2.3. In section 2.4 I continue the way of Scarlata and Panagia resulting in a P-Cygni line profile. In section 2.5 I look at the spectra for different apertures, so on spatial resolved spectra. This is done in (Scarlata and Panagia, 2015) only in a side note and they also did not look in more detail at this topic in the following publications (Carr et al., 2018), (Carr et al., 2021).

2.1 The SALT model to predict the spectra of galactic outflows introduced in the way of Scarlata

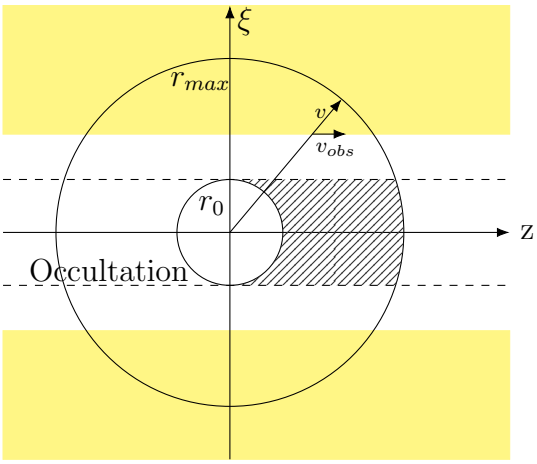

Figure 2.1: Side view of the outflow model of a spherical galaxy of radius r_0 as radiation source (galaxy of star forming region), surrounded by an expanding envelope with an radially increasing velocity up to $v_{\max}$ at $r_{\max}$. The position of an observer is in positive z-direction. The observer sees only the to the line of sight projected velocity v_{obs}.

The model consists of a spherical source emitting radiation up to a radius r_0, which is shown in figure 2.1. The radiation source describes a galaxy or a star forming region. The radiation source is surrounded by a spherical material envelope expanding from r_0 up to $r_{\max}$. The z-axis of the coordinate system is parallel to the line of sight and the ξ-axis is perpendicular to the line of sight. A potential observer is located in the positive direction of the z-axis.
The wind is assumed as a spherical outflow. It is described by a field of velocity as well as a field of density. For the field of velocity a power law of

$$v = v_0 \left(\frac{r}{r_0}\right) \qquad \text{for } r < r_{\max} \tag{2.1}$$

$$v = v_{\max} \qquad \text{for } r \geq r_{\max} \tag{2.2}$$

is assumed. So, the velocity increases with the distance. The outflow starts at the surface of the galaxy with a velocity of v_0 and accelerate up to $v_{\max}$ at

a radius $r_{\max}$.
In spherical outflows, as assumed in this model, a well known P-Cygni line profile appears, which is described in the section 1.5. The profile consists of an absorption and emission component.
The absorption component is created in front of a continuum, between the source and the potential observer. In an outflow each component has a systemic velocity, which is connected to a certain transition and frequency. While the material is absorbing photons, it moves towards the observer. Due to the Doppler effect, the frequency of the transition is blueshifted depending on the velocity of the absorbing material. So the absorption line profile is blueshifted. The asymmetry of the absorbing component depends on the density profile of the absorbing material as well as on the velocity field.
The emission component is produced by re-emitted photons, which are scattered in the line of sight (z-axis) of an observer. The emission is centered at the systemic velocity of the material of the observed component. The re-emitted photons in the shells moving toward the observer are blueshifted compared to the systemic velocity. The re-emitted photons in the shell moving away from the observer are redshifted due to the Doppler effect.

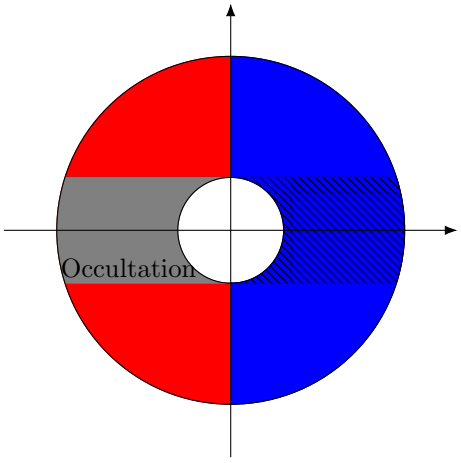

Figure 2.2: In this figure an observer sits on the right. The absorption component is blueshifted due to the Doppler effect. Absorption is observed in the dashed region. The parts of the emission moving towards the observer are blueshifted and the parts of the shells moving away are redshifted compared to the systemic velocity of the wind material component. The areas behind the galaxy are occulted by the galaxy.

"To reduce the radiative transport of the line photons to a local problem" (Scarlata and Panagia, 2015), the Sobolev approximation is assumed, which

is explained in section 2.3. "While the velocity gradient is large, the photons interact with the absorbing ions in the wind material only at resonance" (Scarlata and Panagia, 2015). This is possible due to the Doppler shift. So it is possible to describe the outflow by thin shells with given velocities v at a certain radii r and an optical depth $\tau(r)$. The optical depth is calculated by

$$\tau(r) = \frac{\pi e^2}{mc} f_{lu} \lambda_{lu} n_l(r) \left[1 - \frac{n_u g_l}{n_l g_u}\right] \frac{r/v}{1 + \sigma\mu^2} \tag{2.3}$$

"with f_{lu} and λ_{lu} as oscillator strength and wavelength of the ul transition, $\mu = \cos(\theta)$ and $\sigma = \frac{d\ln(v)}{d\ln(r)} - 1$" (Scarlata and Panagia, 2015). The description of the optical depth $\tau(r)$ is simplified by assuming that

- "$\tau(r)$ does not depend on the angle θ between the radius and the line of sight" (Scarlata and Panagia, 2015)
- equation 2.1 and 2.2 for the velocity law are still valid
- "the stimulated emission is negligible" (Scarlata and Panagia, 2015), so that $\left[1 - \frac{n_u g_l}{n_l g_u}\right] = 1$
- the mass outflow is constant, this means that $n_l(r) = n_0 \left(\frac{r}{r_0}\right)^{-2-\gamma}$ with n_0 as as density at r_0

These assumptions lead to

$$\tau(r) = \frac{\pi e^2}{mc} f_{lu} \lambda_{lu} n_0 \frac{r_0}{v_0} \frac{1}{\gamma} \left(\frac{r}{r_0}\right)^{-1-2\gamma} \tag{2.4}$$

$$= \tau_0 \frac{1}{\gamma} \left(\frac{r}{r_0}\right)^{-1-2\gamma} \tag{2.5}$$

$$= \tau_0 \frac{1}{\gamma} \left(\frac{v}{v_0}\right)^{\frac{-1-2\gamma}{\gamma}} \tag{2.6}$$

With this assumption and approximation for the optical depth, we can calculate the absorption and emission component of the P-Cygni profile of a spherical outflow, which is done in section 2.4.

2.2 Assumptions of the SALT model

For a model you have to take many assumptions into account. It is a challenge to simplify the calculations and to get a result that predicts the spectra well. For this model the following assumptions are used:

- **Glowing ball:** The galaxy is assumed as a bright shining and glowing sphere.
- **Brightness profile:** No brightness profile is considered.
- **Outflow geometry:** The geometry of the outflow is spherical, so the model is invariant in rotation around the line of sight of an observer.
- **Resonant radiative driven wind:** A resonant radiative driving mechanism as introduced in section 1.4 is assumed for the model.
- **Photon emission:** Photons re-emitted isotropically. By the emission process, photons are arbitrary emitted in all directions.
- **Power law for the velocity field:** A power law for the velocity is assumed. The value of the velocity depends on the distance r from the source to the point of velocity. This relation is described by the equations 2.1 and 2.2.
- **Sobolev approximation:** Photons will interact with the outflow material only once, if the velocity gradient of the expanding outflow is large. They will interact with the outflow material exactly at that point, where the ion is at resonance with the photon due to the Doppler shift of the moving ion (Scarlata and Panagia, 2015). Along the line of sight each velocity appears once. So you can transform the spatial coordinates in z-direction explicitly in velocity space. The importance of this assumption is explained in more detail in chapter 2.3.
- **Single scattering:** Re-emitted photons escape a given shell without further interactions. Photons get absorbed by the ions at resonance. After a certain lifetime the excited electron de-excites and emits a new photon. While the lifetime and de-excitation time, the ion moved further in the velocity field, because of the moving shells. The re-emitted photons are then out of resonance and can not interact further with the wind material.
- **Optical depth:** The optical depth is simplified. It is assumed that the optical depth is totally symmetric, so that the optical depth does not depend on the angle between radius and line of sight. Also stimulated emission is neglected to simplify the optical depth. A constant mass outflow is assumed.
- **No fluorescent emission:** A two level atom is assumed with no fluorescent channel.

2.3 Sobolev approximation to reduce radiation transport to a local problem

The Sobolev approximation is assumed in the SALT model. The the theory behind the Sobolev approximation is explained in (Grinin, 2001). In the following this is summarized, up to the discussion of the isovelocitylines.
Since the 1930s it was clear that it is necessary to develop a theory for the formation of spectral lines in a moving media. Without a solution of this question it would be impossible to analyse and characterize the stellar spectra, which show emission lines, which are created by "internal motions of the emitted gas" Grinin (2001). It was one of the most complex problems in the stellar spectra theory that had to be solved.
At this time computers were not available. Theoreticians had to find solutions based on analytical methods.
Summarized in the short monograph "Moving Envelopes of Stars", Viktor Viktorovich Sobolev (Sobolev, 1960) showed a method to solve the complex problem of radiative transfer at the frequencies of spectral lines in a media moving away with a radial velocity gradient. "Attempts to obtain an analytical solution of the problem for moving shells of arbitrary optical depth" (Grinin, 2001) were not successful. Sobolev did not try to get an exact solution. He found an approximative method, which gets more accurate for larger velocity gradients in the medium. Other names for the Sobolev approximations are sometimes high-velocity approximation and supersonic approximation.
The Sobolev approximation is used in many astrophysical problems and is still used nowadays frequently, although it would be possible to calculate some of the astrophysical problems without this approximation numerically.
The main point of the Sobolev approximation is that, due to the Dopplers shift between the "frequencies of the emitting and absorbing atoms, the radiative interaction at each point of the medium is determined mainly by its local vicinity" (Grinin, 2001). The photons in the wind material will only interact with the ions at resonance. The absorbing frequency for the ions is different depending on the velocity of the ion due to the Doppler effect. Due to a large velocity gradient the velocities of the ions are spread radially. So photons with a certain frequency have only a certain vicinity, where they can interact with the ions or wind material. So, "the radiative transport of the line photons can be reduced to a local problem" (Scarlata and Panagia, 2015). Therefore the absorption frequencies are connected to a local vicinity. Trough the Sobolev approximation the spatial coordinates in observation direction are bijective connected to the frequency axis. So, it can easily be transformed and changed between spatial space and frequency space in observation direction.

To visualize the legitimation of the Sobolev approximation and to get an idea to think of this approximation, it is helpful to look on the isovelocitylines. In figure 2.3 we look at our centered spherical galaxy and the surrounding accelerated wind material and look at the areas of same velocity. For a side view on the model these areas appear as lines. For the assumed velocity law in equation 2.1 and 2.2 the iosvelocitylines can easily calculated for different values of γ.

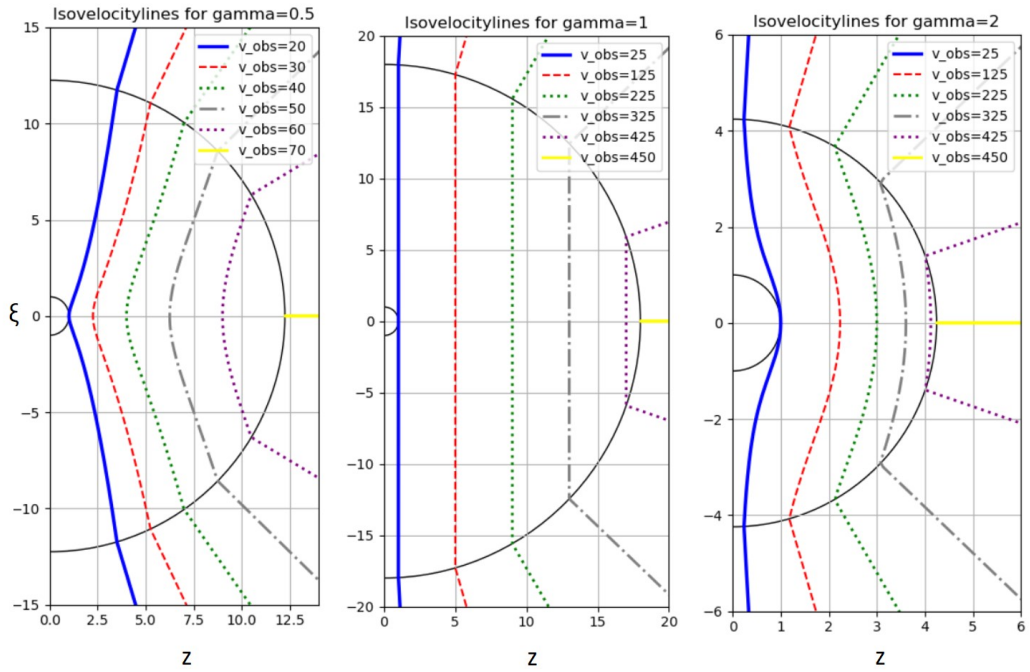

Figure 2.3: Isovelocitylines in the spherical outflow model. The observer sits far away from the object in positive z-direction. A side view of the model is presented, so, areas of same velocity appear as lines of same velocity. We look on the observed velocities v_{obs}. These are the velocities projected to the line of sight, which an observer would see. For $\gamma = 1$, we gain plane lines (middle figure). For values higher or lower, we get shaped lines (left figure for $\gamma = 0.5$ and right figure for $\gamma = 2$). The lines for different velocities do not cross each other, so with knowledge of the velocity law, the position can exactly be connected to a certain velocity value.

For each row is each value of velocity exactly connected to a value on the spatial axis in observation direction. The isovelocitylines do not cross each other and so you can be bijective transform between space and frequency respectively, because frequency and velocity of the moving material are

connected through the Doppler effect.

2.4 Resulting P-Cygni line profile for a galactic outflow in the SALT model

When doing observations of objects in space, the telescope or observer does not see the real velocities. Only velocities, which are projected to the line of sight,

$$v_{\text{obs}} = v \cdot \cos(\theta) = v\frac{z}{\sqrt{z^2 + \xi^2}} \tag{2.7}$$

are observed. By using the in section 2.1 introduced model with all assumptions mentioned in 2.2, it is possible to calculate the impact on the observed spectrum for each observed velocity v_{obs}. For each impact all shells that absorb and re-emit at this observed velocity are considered. The spectrum, which is calculated by the SALT model, results in a P-Cygni line profile. The P-Cygni profile consists of an absorption component and an emission component.

2.4.1 Absorption component of the outflow

Only the part of each shell in front of the radiation source contributes to the absorption spectrum. Absorption can only be observed in front of a continuum source.
The energy fraction

$$E(v) = (1 - \exp(-\tau(v))) \tag{2.8}$$

is absorbed by the shell with velocity v. For a given shell with a certain velocity v and a certain amount of absorbed energy, the energy will be distributed in the range of v_{min} to v. v_{min} is the projection of the velocity along the line of sight tangential to the galaxy. By setting $y = v/v_0$,

$$y_{\text{min}} = \frac{v_{\text{min}}}{v_0} = y \cdot \cos(\theta) \tag{2.9}$$

$$= y^{\frac{\gamma-1}{\gamma}} \left(y^{\frac{2}{\gamma}} - 1\right)^{\frac{1}{2}} \tag{2.10}$$

can be computed. All shells with velocities from v_{obs} up to $v_1 = v_{\text{obs}}/\cos(\theta)$ contribute to the absorption at v_{obs}. By setting $x = v_{\text{obs}}/v_0$ and $y_1 = v_1/v_0$

we can solve the equation

$$y_1^2 \left(1 - y_1^{-\frac{2}{\gamma}}\right) = x^2 \tag{2.11}$$

to get y_1. The absorption profile can be calculated by

$$I_{\text{abs,blue}}(x) = 1 - \int_{\max(x,1)}^{y_1} \frac{1 - e^{-\tau(y)}}{y - y_{\min}} dy. \tag{2.12}$$

The lower boundary of the integral excludes the areas inside the radiation source. The asymmetry occurs from radial differences in density.

2.4.2 Emission component of the outflow

For positive observed velocities the emission line profile is redshifted and for negative observed velocities the emission line profile is blueshifted. In the red component there is an occultation by the galaxy. So all parts of all shells where the location of v_{obs} is occulted, have to be excluded. Thus, to a given v_{obs} only shells with velocities from y_1 up to $y_{\text{inf}} = v_{\max}/v_0$ contribute to the red emission component. The resulting red emission profile can be calculated by

$$I_{\text{em,red}}(x) = \int_{y_1}^{y_\infty} \frac{1 - e^{-\tau(y)}}{2y} dy. \tag{2.13}$$

In the blue emission component there are no parts occulted, only the source of radiation has to be excluded. The blue emission profile can be calculated by

$$I_{\text{em,blue}}(x) = \int_{\max(x,1)}^{y_\infty} \frac{1 - e^{-\tau(y)}}{2y} dy. \tag{2.14}$$

2.4.3 Entire spectrum of the outflow resulting from the SALT model

The entire spectrum results in

$$I(x) = I_{\text{abs,blue}}(x) + I_{\text{em, blue}}(x) + I_{\text{em,red}}(x). \tag{2.15}$$

The resulting spectrum shows a P-Cygni line profile, which is also shown in figure 2.4. Such a P-Cygni profile appears in the spectrum of objects with an outflow.

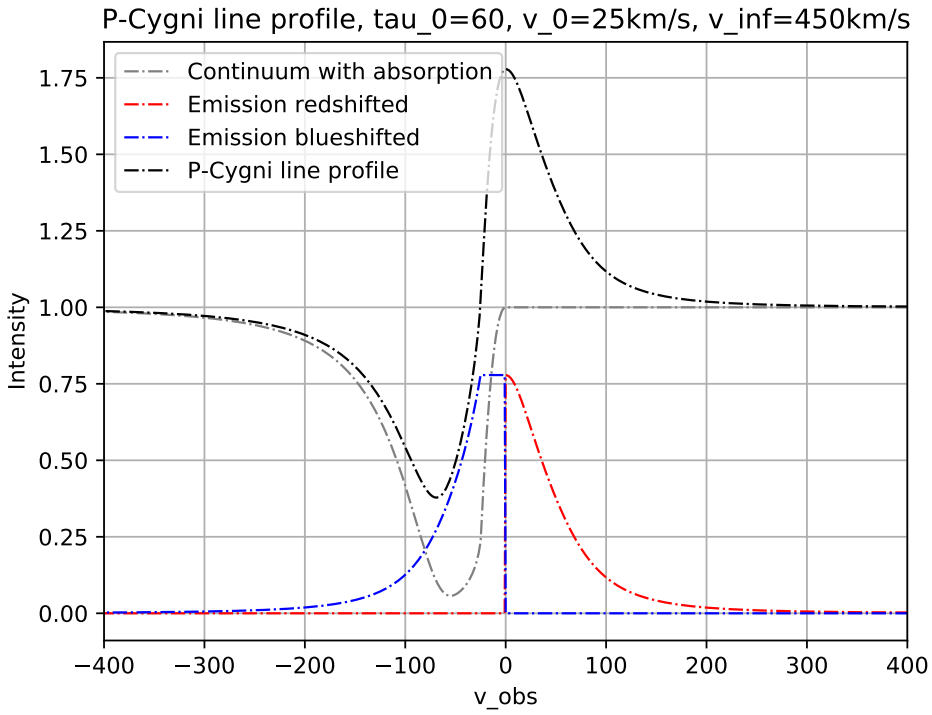

Figure 2.4: Absorption and emission of the SALT model as well as the complete P-Cygni profile, reimplemented in Python. We get a characteristic P-Cygni line profile with a dip and a peak, which is always a good hint for an outflow.

2.5 Spatial resolution of the spectrum with apertures

In (Scarlata and Panagia, 2015) they obtained spatial resolved spectra by implementing apertures (an other way to obtain spatial resolved spectra is introduced in chapter 3).
The apertures do not see the whole extended outflow, they consider only the impact of the outflow on the spectra up to a certain maximum radius. The formalism remains the same, only the upper integration limit changes to

$$y_{\mathrm{up}}^2 = x^2 + \left(\frac{r_{\mathrm{aper}}}{r_0}\right)^2 . \tag{2.16}$$

By implementing different sizes of apertures we get the spectra shown in figure 2.5. For apertures greater than the size of the observed object, the absorption

component remains the same. The smaller the aperture size r_{aper} compared to the outflow size r_{max}, the more the emission component decreases. The more of the emission parts are considered, the more the absorption component gets "filled" by the blueshifted part of the emission component. It is also

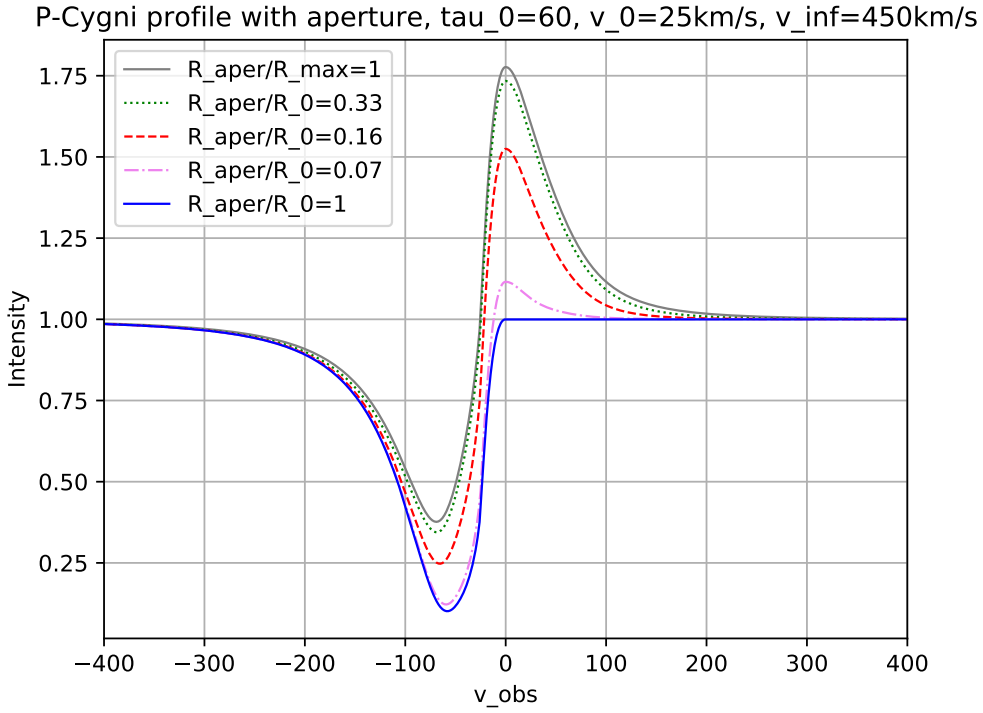

Figure 2.5: The P-Cygni line profile for a linear velocity law ($\gamma = 1$) and different sizes of aperture.

interesting to see, how the P-Cygni profile looks for different velocity laws. This is shown in figure 2.6 for $\gamma = 0.5$ and $\gamma = 2$. There are only small differences for small apertures compared to the profiles for $\gamma = 1$.

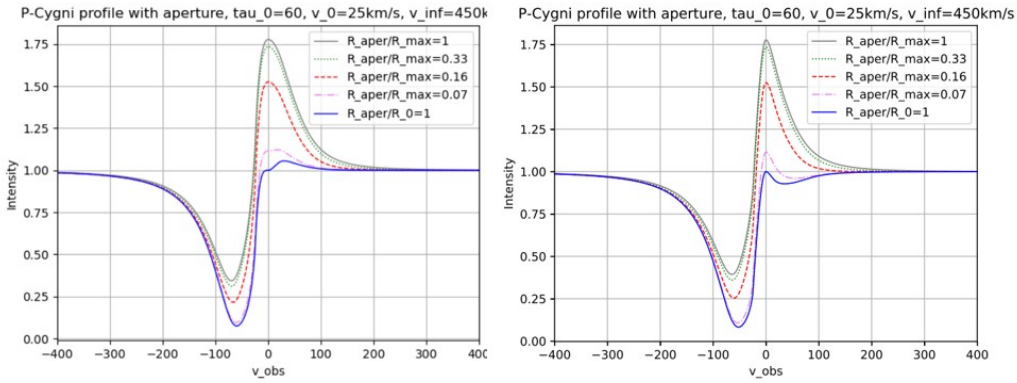

Figure 2.6: On the left: The P-Cygni line profile for a squarerooted velocity law ($\gamma = 0.5$) and different sizes of aperture. On the right: The P-Cygni line profile for a quadratic velocity law ($\gamma = 2$) and different sizes of aperture.

Chapter 3

3D Datacube for galactic outflows

With the SALT model the spectrum of a whole outflow can be predicted well. The **M**ulti **U**nit **S**pectroscopic **E**xplorer (MUSE) measures not only the spectrum of the object. MUSE delivers spatially resolved spectra of the object with an outflow. Since MUSE, there are 3D datacubes of the observed objects available. The data contain of two dimensions in spatial and one dimension in spectral. So it would be nice to have a model to calculate such 3D datacubes. This delivers the opportunity to compare the measured data with the model spatially resolved. Therefore, the model of Scarlata is assumed and transferred to calculate numerically 3D datacubes of outflows.
In this chapter, the focus is on the instrument MUSE and the creation of datacubes. After highlighting the uniqueness of the data measured by MUSE in section 3.1, it is described how datacubes can be generated for the galactic outflow model in section 3.2. After comparing the spectrum from the datacube with the spectrum from the Scarlata model (extended discussion on the difference in chapter 4) in section 3.2.2, it is described how to prepare the extracted spectra from the datacube for comparison with real data in section 3.2.3. In section 3.3 there is a short look on the measured data of the MgII spectral line in the galaxy UDF884. The chapter concludes with a parameter discussion for fitting the model on real data in section 3.4.

3.1 Measurement principle for spatial resolved spectra by MUSE

MUSE is a second generation 3D field spectrograph. A spectrograph analyses light data and is a fundamental tool in astronomy. It was invented in the

1900 century. So this technique is well established. In 1990 the integral field spectrograph, also 3D field spectrograph, was invented in Europe. The first generation was working at the VLT in Chile.
The ESO in Chile has four large telescopes with each a mirror of 8.2 diameter and many first generation 3D field spectrographs. About every ten years a better camera is built and it takes additional five to ten years to built it on a telescope.
MUSE, the **M**ulti **U**nit **S**pectroscopic **E**xplorer, is a second generation 3D field spectrograph. Through MUSE it is possible to observe the very distant universe like in no measurement before. A wide range of sky with many light sources is covered and for each area of the sky a own spectrum is observed. In 2010, the first light was observed by MUSE. This was 13 years after the project start[1].
MUSE measures data for research work on the topics like formation of galaxies, nearby galaxies, stars and resolved stellar populations.
MUSE is supported by seven European research institutes (Bacon et al., 2010):

- Centre de Recherche Astrophysique de Lyon (leading institute)
- European Southern Observatory (ESO)
- Astrophysikalisches Institut Potsdam
- Leiden Observatory (NOVA)
- Laboratoire d'Astrophysique de Toulouse-Tarbes
- Institut für Astrophysik of Gottingen
- Institute for Astronomy at ETH

"MUSE is a wide-field optical integral field spectrograph (IFS) operating in the visible wavelength range with improved spatial resolution" (Bacon et al., 2010). MUSE does imaging and spectrography at the same time. So we gain two dimensions in position space on the sky and one dimension in wavelength or frequencies respectively as shown in figure 3.1.

[1] https://www.eso.org/public/videos/ann17025a/?lang

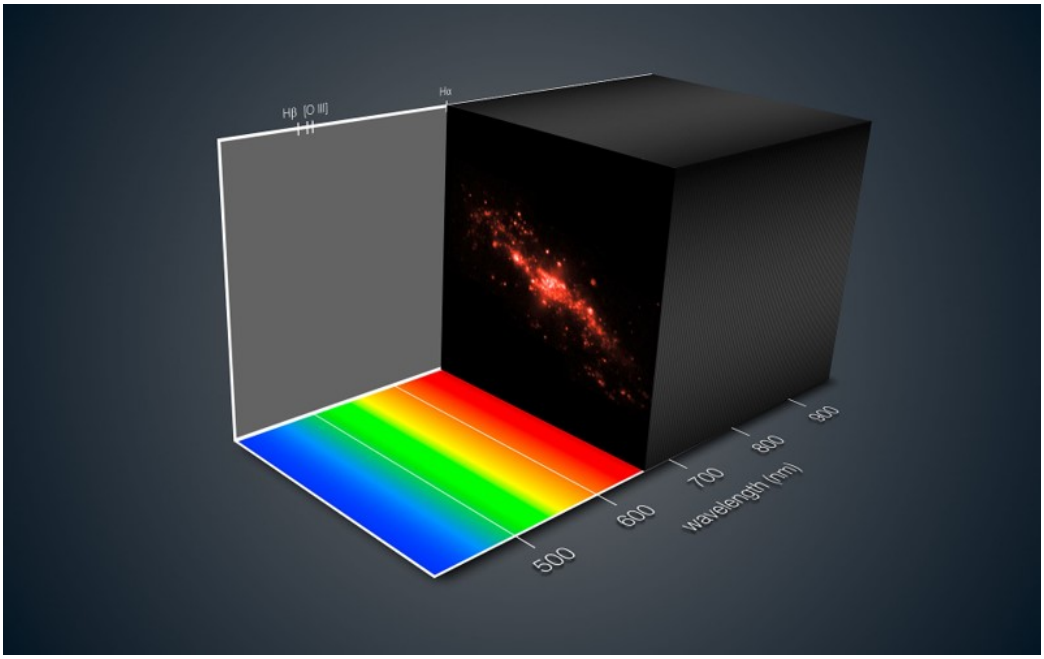

Figure 3.1: The data observed with MUSE are 3D datacubes. They contain information in two dimension in spatial and one dimension in spectral[2].

The sky is observed in the following way: The light enters the instrument. The first optical element for the light is a derotator, which decomposites the earth rotation. This stabilized image is magnified by a pair of mirrors. The beam enters the first field splitter. There the image gets split in 24 slices and we gain 24 separate optical beams. These 24 beams are distributed by mirrors and lenses to the 24 modules. There the light is again split by a second field splitter. This second field splitter, also so called "slicer", is the centrepiece of MUSE. In this slicer the beam is split into 48 slices, so called mini-slits. Each mini-slit has a size of 15 arcsec to 0.2 arcsec. This leads to a total of 1152 such mini slits. Each small light beam is reflected by mirrors and enters the spectrograph. So the detector registers the spectrum of a small part of the galaxy. This process is repeated for each of the 48 small beams and is simultaneous done in each of the 24 modules. All in all it results in a pixeled image, which contains the spectrum information of every region of the galaxy[3][4] (Bacon et al., 2010). The splitting process is schematic shown

[2] https://en.wikipedia.org/wiki/Multi-unit_spectroscopic_explorer#/media/File:MUSE_views_the_strange_galaxy_NGC_4650A.jpg

[3] https://www.eso.org/public/videos/ann17025a/?lang

[4] https://www.eso.org/public/teles-instr/paranal-observatory/vlt/vlt-instr/muse/

in figure 3.2.

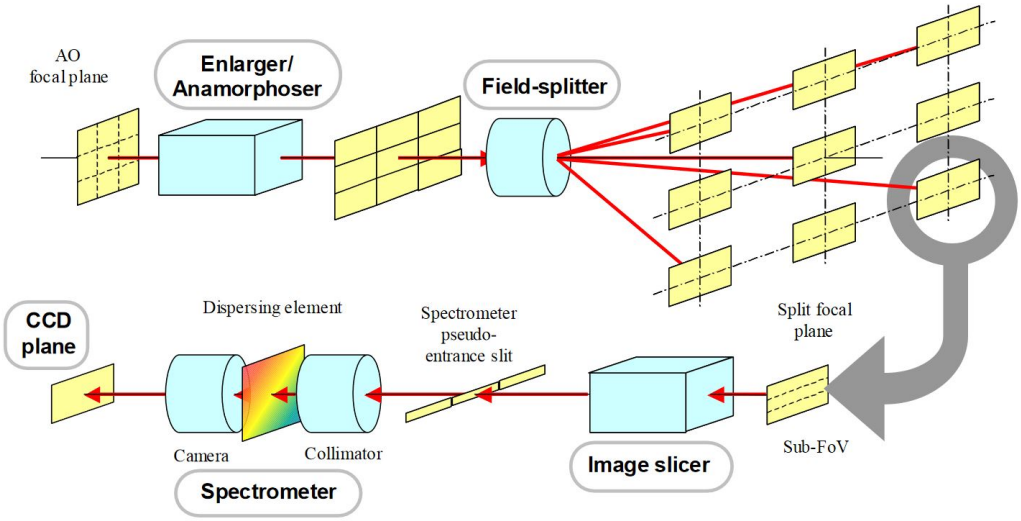

Figure 3.2: The detected light is split up in several areas, which are injected in different spectrometers. Through this splitting process, it is possible to gain spatially resolved spectra of different regions of an object (Henault et al., 2002).

3.2 Calculate spectra of outflows via a 3D datacube

As motivated in section 3.1, the data measured by MUSE are unique. It is possible to obtain 3D datacubes with spatially resolved spectra of an object. It would be useful to have a model that creates similar datacubes, from which we can extract the spectrum for a selected region. The datacube has three dimensions, two spatial coordinates x and y in the plane of the observer and one spatial dimension z respectively one spectral dimension $w = \frac{v}{v_0}$ in the direction of the observer. For faster calculation it is useful to use directly the w-coordinate, because then we have not to interpolate the data before extracting the spectrum and so we need less calculation power.
First, we calculated the velocity

$$v = v_0 \left(\frac{r}{r_0} \right)^{\gamma} \tag{3.1}$$

for each coordinate point in our datacube. We do this in the following explanation for the case $\gamma = 1$. This is visualized in an imshow map on the

left side in figure 3.3. Then we calculate the observed velocity

$$v_{\text{obs}} = v \cdot \cos(\theta) = v \frac{z}{\sqrt{\xi^2 + z^2}}, \tag{3.2}$$

which is the velocity projected on the line of sight. This value of velocity sees a potential observer far away of the observed object. As shown on the right in figure 3.3, the velocities in the front part of the object, which move towards the observer, are blueshifted. The velocitys in the parts of the wind moving away are redshifted.

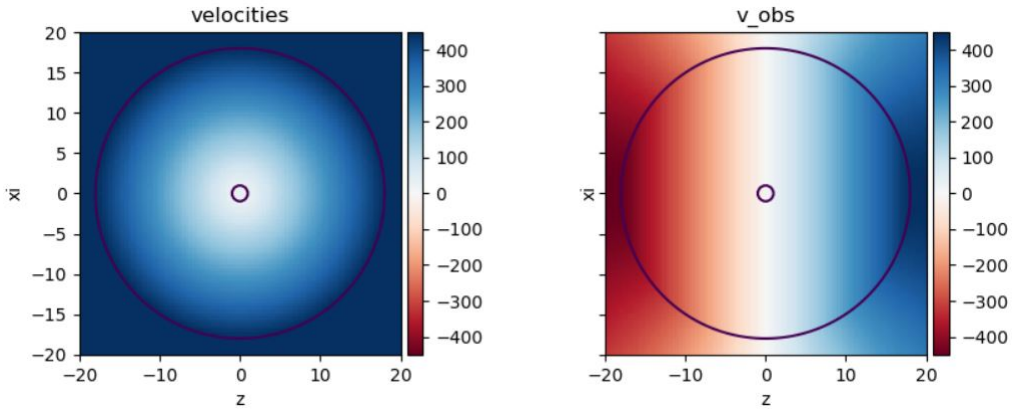

Figure 3.3: The inner circle describes the size of the galaxy. The wind material gets accelerated up to a certain radius (outer circle), which is shown in the left figure. On the right the observed velocity is shown in the case that an observer is far away of the galaxy in positive z-direction. In the presented side view, we see that the velocities of components moving towards the observer are blueshifted and the velocities of components moving away from the observer are redshifted due to the Doppler effect.

The next step is to calculate which impact each coordinate has on the spectrum. Therefore, we create a datacube for the absorption as well as for the blue- and redshifted emission. The absorption impact of each coordinate is calculated by

$$I_{\text{abs,blue}}(s, \xi) = \frac{(1 - e^{-\tau(r)})}{\pi r_0^2} \cdot \mathrm{d}x \cdot \mathrm{d}y \tag{3.3}$$

and there is only absorption in between the source and the observer, as visualized on the left in figure3.4. As you see, the absorption component gets

scaled by the continuum disc πr_0^2.
For the bluesifted emission we calculate with

$$I_{\text{em,blue}}(s,\xi) = \frac{(1-e^{-\tau(r)})}{4\pi r^2} \cdot \mathrm{d}x \cdot \mathrm{d}y \tag{3.4}$$

the same as for the redshifted emission with

$$I_{\text{em,red}}(s,\xi) = \frac{(1-e^{-\tau(r)})}{4\pi r^2} \cdot \mathrm{d}x \cdot \mathrm{d}y. \tag{3.5}$$

It has to be kept in mind that for the redshifted parts some areas are excluded due to occultation of our object, which is visualised on the right in figure 3.3. The parts of the area, where our object is, have to be excluded in absorption and emission. The emission is scaled by the size of the shell at this radius by $4\pi r^2$.

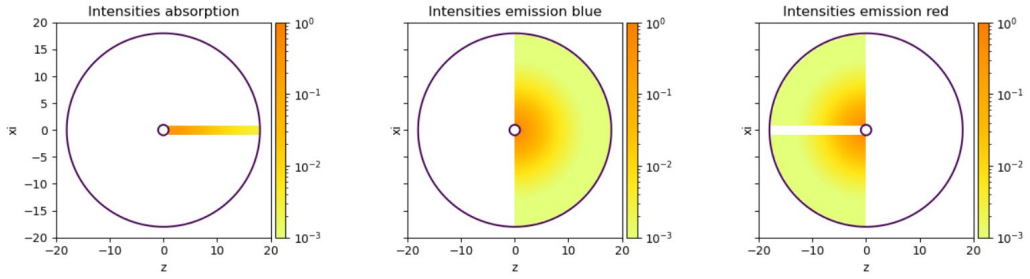

Figure 3.4: Only areas in front of a continuum source contribute to the absorption component of the spectrum (left figure). In the blueshifted emission component the radiation source, e.g. our galaxy has to be excluded (middle figure). In the redshifted emission component there are some parts occulted by the galaxy (right figure).

Now, the final datacube is calculated. By adding all points for each specific observed velocity, we gain the spectrum of this datacube. So all rows are added up and one spectral row remains, which has the intensities for the observed velocities as content. The extracted spectrum of the outflow is a typical P-Cygni line profile, which is also shown in figure 3.5.

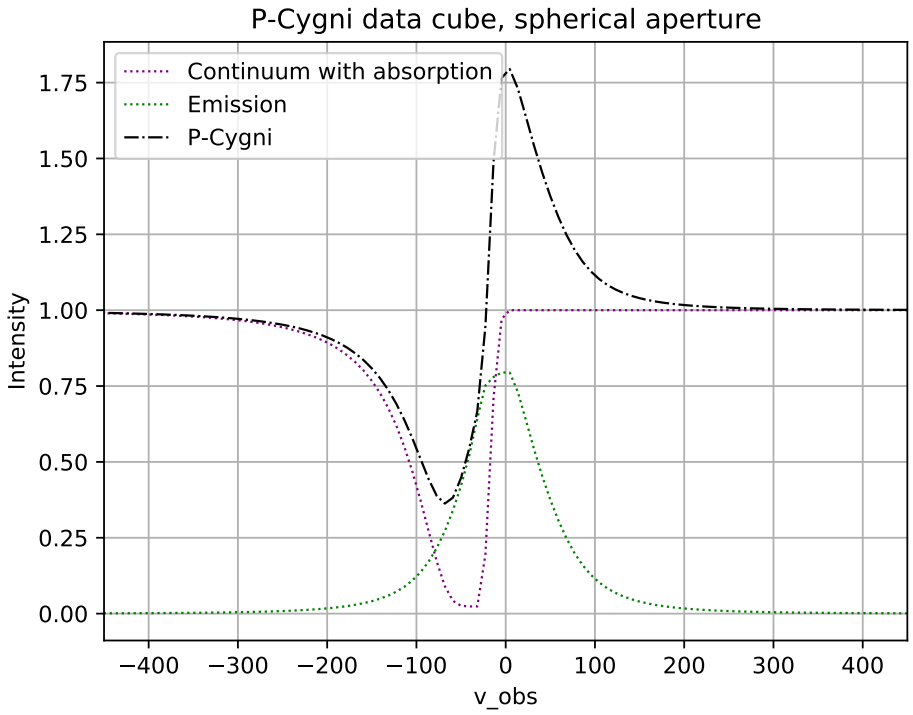

Figure 3.5: From the datacube calculated and extracted spectrum for absorption and emission for a spherical galactic outflow. An expected P-Cygni line profile appears.

3.2.1 Spatial resolution via apertures

Our main interest in these calculated datacubes is to gain spatial resolved spectra. This can be done by selecting only a certain area of the outflow and adding only the parts of absorption and emission in this area together to extract a spectrum for this area. In this thesis it is done for circular apertures, as shown in figure 3.6 and 3.7, as well as for quadratic areas, as shown in figure 3.8.

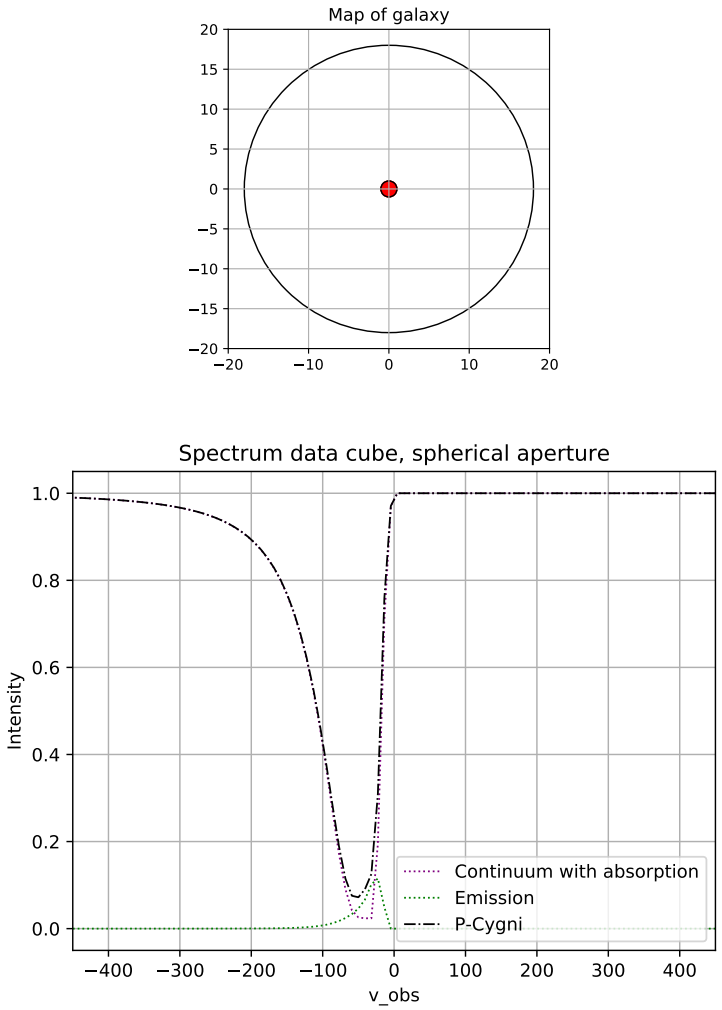

Figure 3.6: In the upper figure the size of the circular centered aperture is shown. The resulting spectrum for a small circular aperture, which is extended to the radius r_0, is shown in the lower figure. Therefore, we see the full absorption component and a small part of the blueshifted emission component. The redshifted emission component is completely occulted at a such small aperture size.

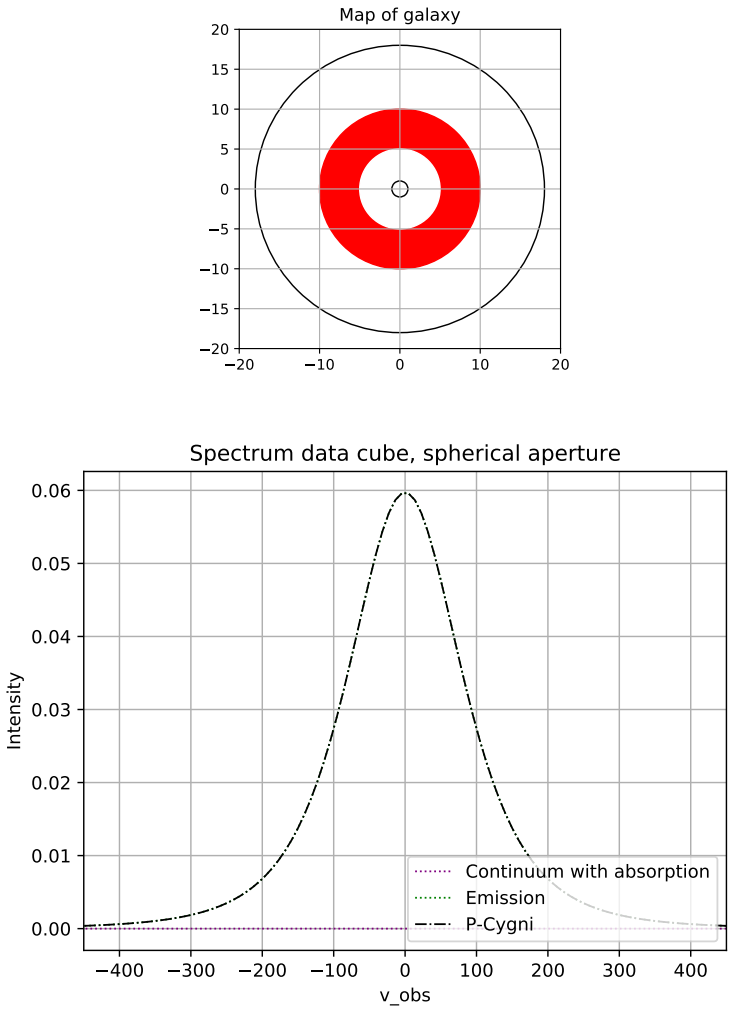

Figure 3.7: In the upper figure the size of the ring centered aperture is shown. The resulting spectrum for a ring aperture, which is extended from $r = 5\frac{r_{\max}}{r_0}$ to the radius $r = 10\frac{r_{\max}}{r_0}$, is shown in the lower figure. Therefore, we see no absorption component, because the aperture covers not the galaxy and so not the area, where absorption can be detected. A small part of the blueshifted emission component and the redshifted emission component is detected and results in the observed spectrum.

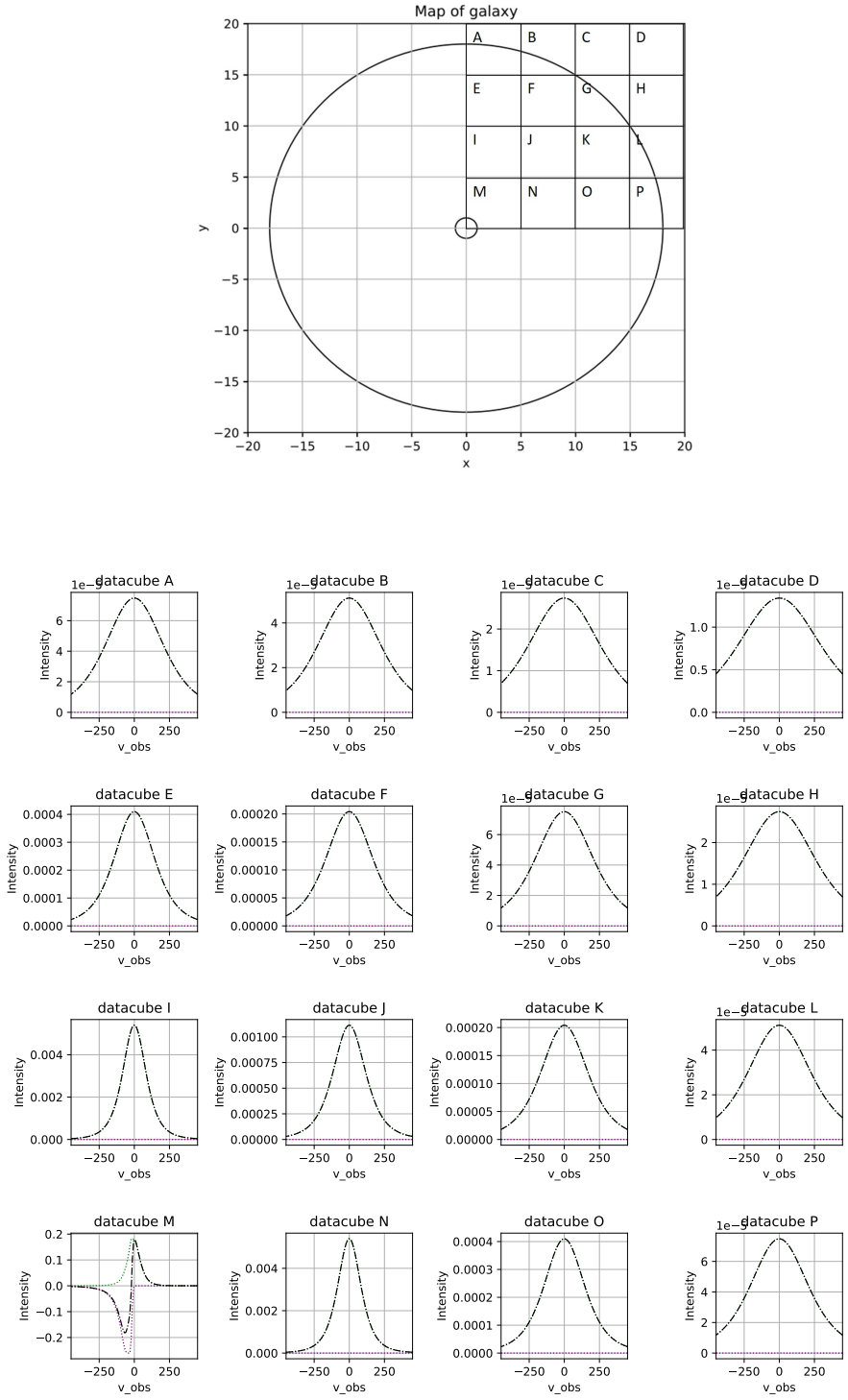

Figure 3.8: In the upper figure the areas for the calculated spectra are shown. In the lower figure the extracted spectra are shown. The emission component decreases for outer parts. Absorption is only detected in the inner part (datacube M) in front of the galaxy.

3.2.2 Comparing the spectrum calculated by the datacube and the spectrum calculated by Scarlata

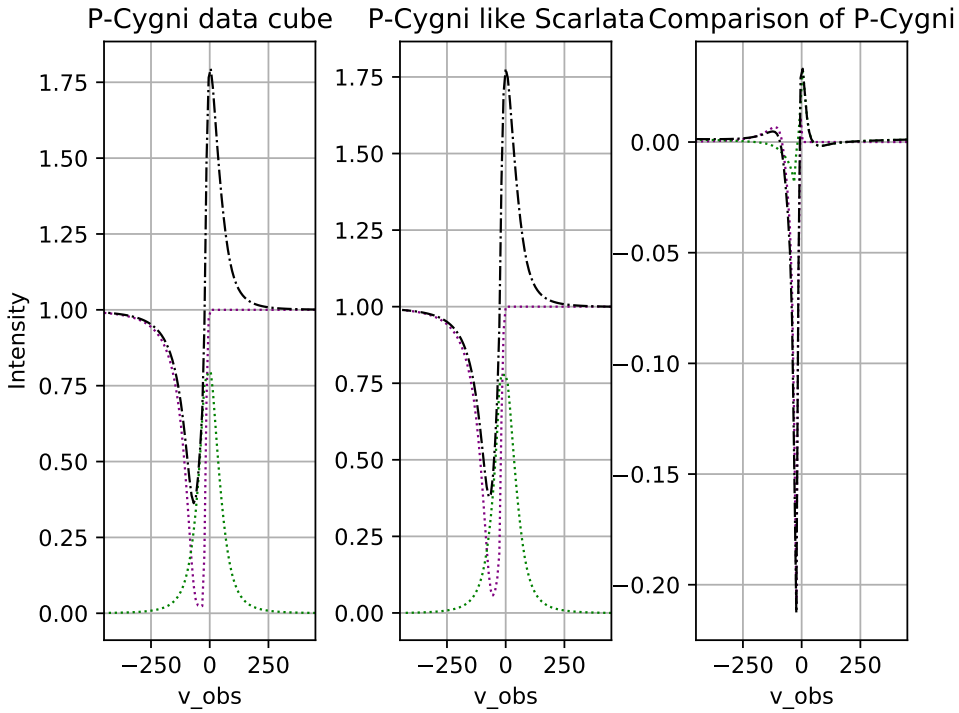

Figure 3.9: On the left the P-Cygni line profile, as well as absorption and emission are shown, which are calculated by the datacube. In the middle the P-Cygni line profile, as well as absorption and emission are shown for the model of Scarlata. On the right figure is the comparison of both models. The emission component is pretty similar, despite the fact of uncertainties in the numerical calculation. In the absorption component occurs a big difference. This does not get smaller for more datapoints in the datacube. The reason for the difference between the both calculations is discussed in chapter 4.

It is common to test and compare different models, which calculate the same content in different ways. The comparison of the model of Scarlata and of the datacube showed that the emission is similar, despite some numerical uncertainties in the area of small velocities, which is shown in figure 3.9. This error gets smaller for a higher resolution of datapoints in the datacube. In the absorption component a big difference occurs, which can not be lowered by higher resolution of the datacube. This is a hint, that something went

wrong in one of the two models. This difference, as well as an approach how the error can be fixed, is discussed in chapter 4.

3.2.3 Convolution to prepare the model for comparison with real data

Real measured data is not as exact as models with infinite resolution. The data has always a certain uncertainty. The measured data gains a spatial uncertainty, because the light measured with MUSE on earth went trough the atmosphere. The data gets also a spectral uncertainty in the interferometer. To compare the modelled data with the measured data, we have to convolve the data first in spatial xy-direction with a 2D Moffat profile of

$$\left[1 - \left(\frac{r}{\alpha}\right)^{\beta}\right]^{-1/2}. \tag{3.6}$$

"The Moffat circular function falls off relatively slow. [...] So a large convolution kernel is needed [...] and therefore it gets more efficient to perform [...] in the Fourier domain" (Bacon et al., 2010). After the spatial Moffat convolution the data gets convolved by a 1D Gaussian kernel in spatial direction.
For the spatial point spread function (PSF) the MUSE data is best described by a Moffat function. Therefore, we can choose β as constant with $\beta = 2.8$. We have a linear decrease of the FWHM with wavelength. We achieve a spatial resolution of 0.71 arcsec at a wavelength of 4750 Å. The spatial resolution decreases down to 0.57 arcsec at a wavelength of 9350 Å.
For the spectral line spread function (LSF) a Gaussian is fitted to each line. The FWHM varies as a function of wavelength with

$$F_{\mathrm{udf10}}(\lambda) = 5.866 \cdot 10^{-8} \cdot \lambda^2 - 9.187 \cdot 10^{-4} \cdot \lambda + 6.040. \tag{3.7}$$

It is okay to apply a Gaussian spatial smoothing kernel of 0.4 arcsec FWHM. MUSE has a measured standard deviation of only 0.02 arcsec (Bacon et al., 2010).
By the convolution the spectra, calculated by the datacube model, get smeared out as shown in figure 3.10. After the convolution of the datacube data, a comparison to measured data is possible.

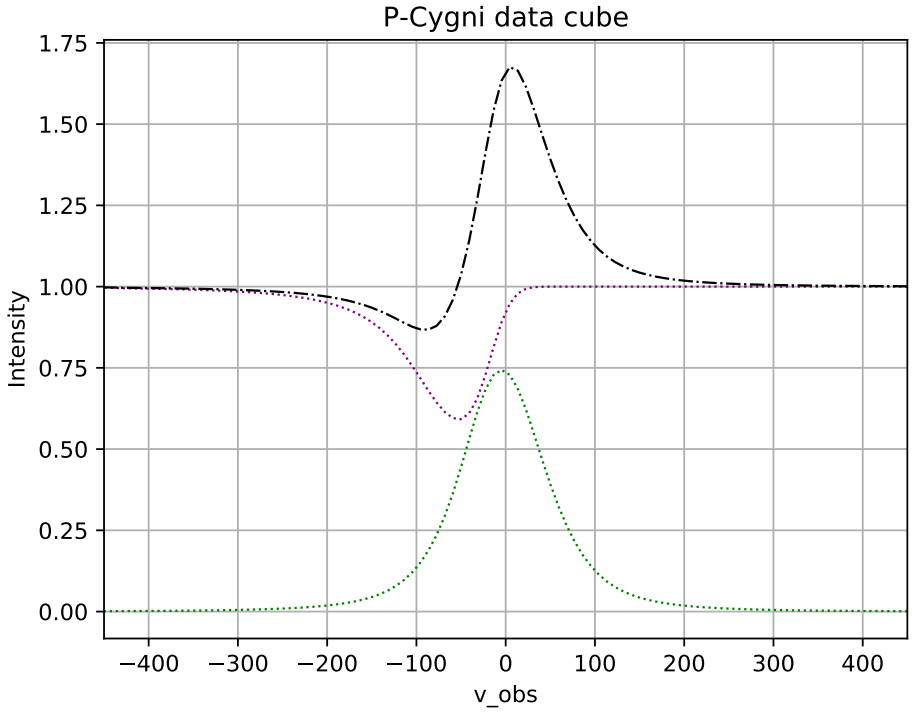

Figure 3.10: To compare the spectra, calculated by the datacube, the data gets convoluted by a PSF in spatial dimension and a LSF in frequency dimension. The spectrum smears out through these convolutions.

3.3 Spectra of the galaxy UDF884 with a sperical outflow for different aperture sizes

We look on a galaxy with the internal label "UDF884". We are interested in the spectral line of MgII. MgII is a doublet. The blue line of MgII has a wavelength of 2795.53 Å and the red line 2802.70 Å. The galaxy has a redshift of $z = 0.737$. Therefore, 1 arcsec equals 7.3 kpc.
In the spectra for different apertures (figure 3.11) the data resembles a P-Cygni line profile. There occur two P-Cygni profiles because of the doublet structure of MgII. As mentioned before in the model, for smaller sizes of the spherical aperture the emission component decreases. This trend is also seen in the observed data. For larger aperture sizes it can also be observed that the blueshifted emission component "fills" the absorption component. The data show the same behaviour as the calculated and predicted spectra by the

data cube.

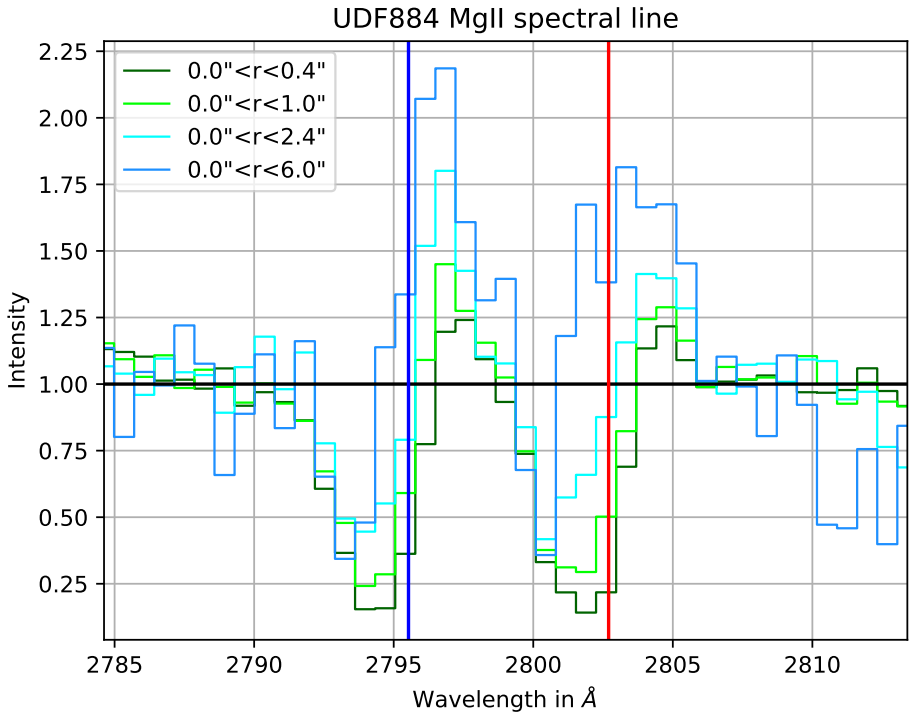

Figure 3.11: We look in the spectrum of UDF884 at the MgII doublet line for different apertures. The apertures are concentric rings with the radii of 0.4, 1.0, 2.4 und 6.0 arcsec. A P-Cygni line profile appears.

3.4 Parameter discussion for the fitting process of the model to measured data

After looking at the observed spectrum of UDF884 for different aperture sizes, it would be useful to fit the spectrum gained by the datacube to the observed data. Aim of this section is to discuss, which parameters in the model can be fixed and which parameters have to stay variable for fitting the model to the measured data in a later step. For less computation power it is good to set most of the parameters to a fixed value and to have only a few parameters that remain variable. In our model we have the following parameters:

- r_0
- $r_{\max}$

- v_0
- $v_{\max}$
- γ
- $\tau\,(r)$

Pictures of the galaxy UDF884 exist like in figure 3.12 shown. From these we can estimate the size of the galaxy r_0. It is difficult to define a fixed radius for a galaxy, because the galaxy has no clear cut and there is rather a smooth transition from galaxy to surrounding medium. However, it should be possible to estimate a galaxy size from images fair enough, to set r_0 as fixed parameter.

The same problem with no clear cut and rather a smooth transition appears

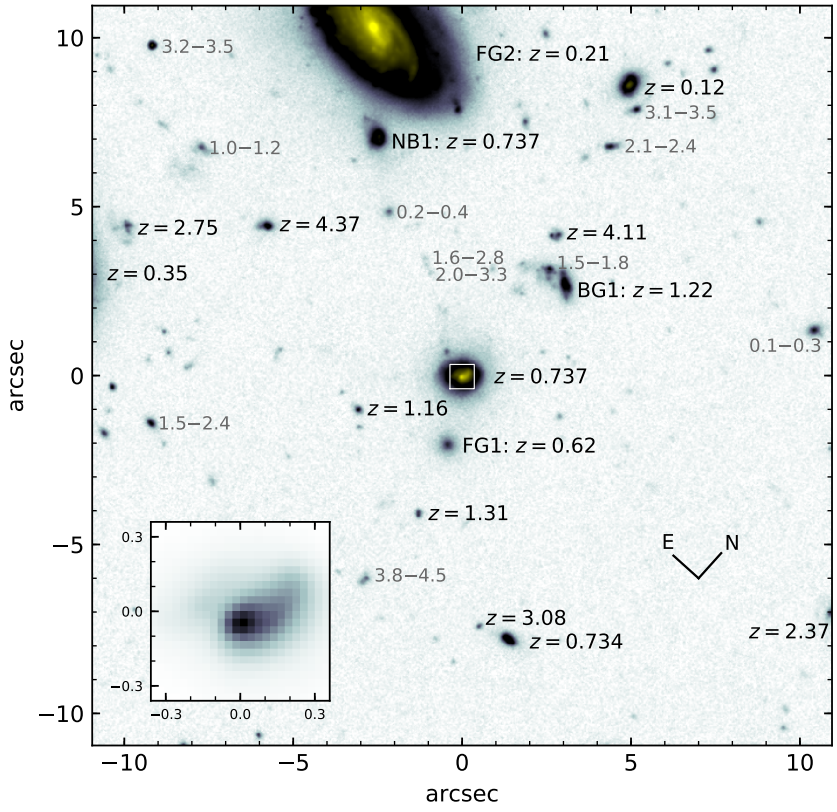

Figure 3.12: A picture of our galaxy UDF884. From this image we can estimate the size of the galaxy (Lutz Wisotzki, 2021).

in the case of $r_{\max}$. There is a smooth transition between the accelerated

wind material and the CGM. We can approximately assume the aperture radius of our observation instrument as $r_{\max}$.
$v_{\max}$ can be estimated by how much the velocity is maximal shifted away from the internal transition of each transition of the two lines of the MgII doublet. So approximately we can manage to set $v_{\max}$ to a fixed parameter.
γ can not be set to a fix parameter through analysing the spectrum. Maybe it is possible to limit γ in a range due to looking at velocity maps. However, the variable γ probably has to remain as a fitting parameter.
By having set r_0, $r_{\max}$ and $v_{\max}$ to a fixed value and having γ as a variable parameter, the variable v_0 results out of these four quantities by assuming the power law for the velocity like introduced in the model in equation 2.1 and 2.2.
The last parameter to have a look at, is $\tau(r)$. By assuming the relation introduced in equation 2.6, there would remain the variables γ and v_0 as variables, which where discussed before and the variable τ_0. It can also be thought of taking not the introduced relation for τ and instead let τ be a variable function in the fitting process on the real data.
All in all, it can be possible to limit the six variable parameters of the model to three variable parameters. By limiting the number of parameters, less calculation power is needed to fit the spectrum extracted from the datacube model on real data.

Chapter 4

What went wrong in the absorption component in the model of Scarlata?

In figure 3.9 the absorption component, emission component and the total P-Cygni line profile of the Scarlata model and the datacube are compared. In the absorption component there occurs a big difference between the model introduced by Scarlata and the datacube.
In this chapter we analyse and discuss, what went wrong in the calculation of the absorption component of the P-Cygni line profile in the model for galactic outflows introduced by Scarlata and Panagia (Scarlata and Panagia, 2015). They referred to the model for stellar outflows introduced by Scuderi (Scuderi et al., 1994). Scarlata and Panagia transfer the error in the calculation of the absorption from the stellar wind model from Scuderi to the outflow model of galaxies.
The ideas discussed in the following sections are mainly developed by Lutz Wisotzki (LW2021), and based on seven pages of handwritten notes. In section 4.6 I will continue with the approach and calculate it in the non scaling-free case. Then, calculations are continued for a variable γ in section 4.7.

4.1 Notation for $\gamma = 1$

The velocity-radius relation

$$\frac{v}{v_0} = \frac{r}{r_0} \tag{4.1}$$

is described by a linear relation in the case of $\gamma = 1$ (compare equations 2.1 and 2.2). In figure 4.1 the coordinates for the model are visualized. A rotation symmetry around the z-axis ($\xi = 0$) is adopted, so the problem is axially symmetric. w describes the normalized projected velocity, which a potential observer will observe and is parallel to the z-axis. It is projected to the line of sight for an observer. In Scarlata x is used instead of w. The following calculations are done in the scaling-free case, which is done by setting $r_0 = 1$ and $v_0 = 1$. The velocity-radius relation is simplified to

$$v = r. \tag{4.2}$$

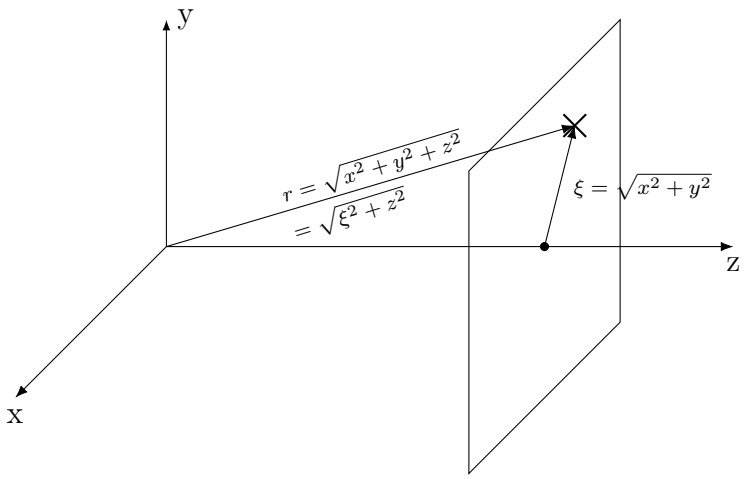

Figure 4.1: The z-axis (in Scarlata: x) is directed to the observer. The x- and y-coordinates are in source plane. Therefore, in source plane you get a projected radius $\xi = \sqrt{x^2 + y^2}$. The distance of a point to the source is described by the radius $r = \sqrt{x^2 + y^2 + z^2} = \sqrt{\xi^2 + z^2}$.

The observed velocity is described by

$$v_{\text{obs}} = v \cdot \cos(\theta) = v\frac{z}{r}, \tag{4.3}$$

which results in

$$v_{\text{obs}} = z \tag{4.4}$$

and the observed velocity normed by $v_0 = 1$ looks like

$$w = \frac{v_{\text{obs}}}{v_0} = z. \tag{4.5}$$

Now, we look only on the absorption component created by the outflow. We do not consider the re-emission component. The absorption component is created in front of a continuum, in our case the absorption component is created in the outflow parts between the source (galaxy or star forming region) and the observer. So for the absorption component it is enough to look only at

$$\xi \leq 1, \tag{4.6}$$

which describes the area covered by the radiation source in the xy-area.
"The monochromatic luminosity of the galaxy is described by $L_w(w)$." (LW2021)
"The flux received by an observer is described by

$$F_w = \frac{L_w}{4\pi d^2} \tag{4.7}$$

with the distance d, which is not relevant here." (LW2021)
As a special case and to test our assumption, we consider for the optical depth

$$\tau \approx \infty. \tag{4.8}$$

In approximation it follows

$$\left(1 - e^{-\tau}\right) \approx 1. \tag{4.9}$$

It does not matter what happens with the optical depth. The problem simplifies to a pure geometric problem. For $w > 1$, the galaxy is invisible and the absorption is complete.

4.2 Spatial integration approach

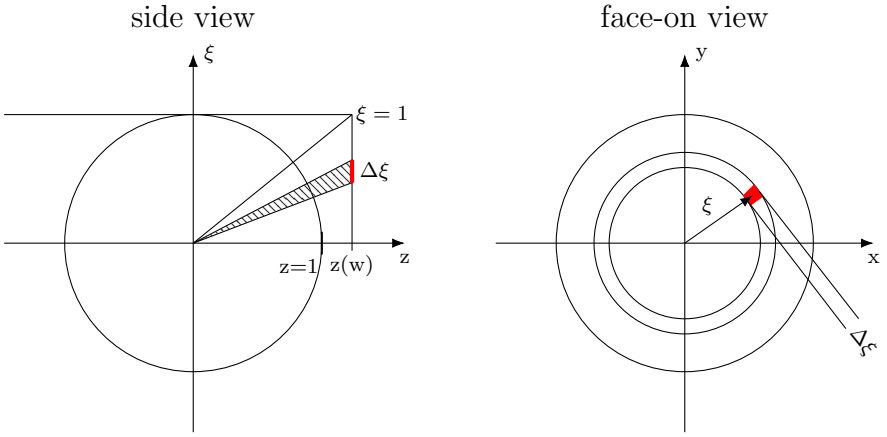

Figure 4.2: Side view on the left and face-on view on the right. It is visualized, which fraction of the galaxy is covered by an annulus.

We look in a face-on view at our galaxy (figure 4.2). We cut out an annulus with radius ξ up to $\xi + \Delta\xi$. We calculate the area of this certain annulus and receive

$$\pi\left((\xi+\Delta\xi)^2-\xi^2\right) \tag{4.10}$$
$$=\pi\left(\xi^2+2\xi\Delta\xi+\Delta\xi^2-\xi^2\right) \tag{4.11}$$
$$\approx 2\pi\xi\Delta\xi \tag{4.12}$$

as the size of the annulus. The annulus covers a part of the galaxy. The fraction

$$\frac{2\pi\xi\Delta\xi}{\pi r_0^2}=\frac{2\xi\Delta\xi}{r_0^2} \tag{4.13}$$

is covered by the annulus. The absorbed spectrum is gained by integration of ξ from 0 up to 1, because this is the complete area in the xy-plane, where absorption happens. For the absorption component we gain the integral

$$F_{\text{absorbed}}(w)=\frac{L_w}{4\pi d^2}\frac{1}{r_0^2}\int_0^1\left(1-e^{-\tau(w,\xi)}\right)\cdot 2\xi\mathrm{d}\xi. \tag{4.14}$$

If we refer to our assumption with an optical depth of $\tau(w)\approx\infty$, the integral can be easily calculated by

$$F_{\text{absorbed}}(w)=\frac{L_w}{4\pi d^2}\frac{1}{r_0^2}\left[\xi^2\right]_0^1=\frac{L_w}{4\pi d^2}\frac{1}{r_0^2} \tag{4.15}$$

and it results in

$$F_{\text{absorbed}}(w) = F^{\text{unabsorbed}}_{\text{circular disk with radius } \xi = 1}(w). \tag{4.16}$$

This states that the flux of the absorption spectrum is the same as the flux of the unabsorbed circular disk with radius $\xi = 1$. If we assume an optical depth of $\tau \approx \infty$ and that the complete area is covered, "there is no possible path for continuum photons to escape" (LW2021) (this is different than by scattering, so when re-emission is taken into account).

4.3 Velocity integration approach

As done in section 4.2 in the spatial approach, the flux can also be calculated in velocity space.
First, we have to transform the variables by

$$v = r = \sqrt{\xi^2 + z^2} = \sqrt{\xi^2 + w^2}. \tag{4.17}$$

For a certain and fixed value of w it leads to

$$\frac{\mathrm{d}v}{\mathrm{d}\xi} = \frac{\frac{1}{2}2\xi}{\sqrt{\xi^2 + w^2}} = \frac{\xi}{v}, \tag{4.18}$$

which results in

$$\mathrm{d}\xi = \frac{v}{\xi} \cdot \mathrm{d}v \tag{4.19}$$

for the variable transformation in the integral. As lower integral limit we get $v(\xi = 0) = w$ and as upper integral limit $v(\xi = 1) = v_1 = \sqrt{1 + w^2}$. The absorbed spectrum results in

$$F_{\text{absorbed}}(w) = \frac{L_w}{4\pi d^2}\frac{1}{r_0^2}\int_0^1 \left(1 - e^{-\tau(w,\xi)}\right) \cdot 2\xi \mathrm{d}\xi \tag{4.20}$$

$$= \frac{L_w}{4\pi d^2}\frac{1}{r_0^2}\int_w^{\sqrt{1+w^2}} \left(1 - e^{-\tau(w,\xi)}\right) \cdot 2\xi\frac{v}{\xi}\mathrm{d}v \tag{4.21}$$

$$= \frac{L_w}{4\pi d^2}\frac{1}{r_0^2}\int_w^{\sqrt{1+w^2}} \left(1 - e^{-\tau(w,\xi)}\right) \cdot 2v\mathrm{d}v \tag{4.22}$$

We can test the calculation for the case $\tau \approx \infty$ and get

$$F_{\text{absorbed}}(w) = \frac{L_w}{4\pi d^2}\frac{1}{r_0^2} \cdot \left[v^2\right]_w^{\sqrt{1+w^2}} \tag{4.23}$$

$$= \frac{L_w}{4\pi d^2}\frac{1}{r_0^2}\left(\left(1 + w^2\right) - w^2\right) \tag{4.24}$$

$$= \frac{L_w}{4\pi d^2}\frac{1}{r_0^2} \tag{4.25}$$

which results in the same result and interpretation as in section 4.2.

4.4 Velocity integration approach by Scarlata/ Scuderi

The absorption component appears as

$$\frac{F_{\text{absorbed}}(w)}{F^{\text{unabsorbed}}_{\text{circular disk with radius } \xi=1}(w)} = \int_{\max(w,1)}^{\sqrt{w^2+1}} \frac{\mathrm{d}v}{v-\sqrt{v^2-1}} \tag{4.26}$$

introduced by Scarlata respectively by Scuderi for the case $\gamma = 1$. If we test the equation by taking $w = 1$ and assuming $\tau \approx \infty$, we get

$$\frac{F_{\text{absorbed}}(w=1)}{F^{\text{unabsorbed}}_{\text{circular disk with radius } \xi=1}(w=1)} = 0.766 \tag{4.27}$$

by integrating numerically instead of 1. This is "impossible! As we have seen [in section 4.2 and 4.3,] there is no way that continuum gets through. Generally, this formula gives systematically too low absorption. [However,] it converges for $w \to \infty$." (LW2021)

4.5 What went wrong in Scarlata/Scuderi?

4.5.1 Manipulating the correct formula

In this section we manipulate our correct formula introduced in section 4.2 and 4.3 to get the incorrect equation introduced in 4.4.
If we compare the different versions

$$\int_{w}^{\sqrt{1+w^2}} \left(1-e^{-\tau(w,\xi)}\right) \cdot 2v\mathrm{d}v \tag{4.28}$$

(our approach) and

$$\int_{\max(w,1)}^{\sqrt{1+w^2}} \left(1-e^{-\tau(w,\xi)}\right) \frac{\mathrm{d}v}{v-v_{\min}} \tag{4.29}$$

(Scarlatas approach), with $v_{\min} = \sqrt{v^2-1}$, still for the case $\gamma = 1$, we find the difference in the above mentioned red coloured parts of the integrands.

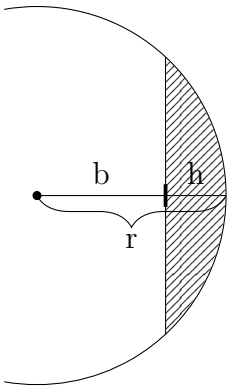

Figure 4.3: Surface of a spherical shell segment of the outflow.

In figure 4.3 the surface of a spherical shell segment is visualized. The surface of a spherical shell segment can be calculated by

$$S = 2\pi r h \tag{4.30}$$

where $h = r - b$. A "surface of a single shell [(with fixed ring with $\mathrm{d}z$)] contributes to this segment [by the amount of] [...]

$$\mathrm{d}S = 2\pi r \mathrm{d}z \tag{4.31}$$

and does not depend on the value of z or ξ" (LW2021), which may be surprising.
We expand our integrand 4.28 in our approach by

$$\frac{\pi h}{\pi h} \tag{4.32}$$

where

$$h = r - \sqrt{r^2 - 1} = r - r_{\min} \tag{4.33}$$
$$= v - \sqrt{v^2 - 1} = v - v_{\min} \tag{4.34}$$
$$\tag{4.35}$$

for $\gamma = 1$. Therefore, we gain

$$\frac{2v}{r_0^2} = \frac{2v}{r_0^2}\frac{\pi h}{\pi h} \tag{4.36}$$

$$= \frac{2\pi r h}{r_0^2 \pi h} \tag{4.37}$$

$$= \frac{2\pi r h}{\pi r_0^2}\frac{1}{h} \tag{4.38}$$

$$= \frac{2\pi r h}{\pi r_0^2}\frac{1}{r - r_{\min}} \tag{4.39}$$

as part of the integrand. The first fraction in equation 4.39 is a "correction factor" and describes

$$\frac{2\pi r h}{\pi r_0^2} = \frac{\text{fraction of covered area of shell segment between } \xi = \pm 1}{\text{area of cross section } r_0 = 1}. \tag{4.40}$$

4.5.2 Forward approach: Pinpointing the error

We quote (Scuderi et al., 1994) p. 203 by

> "The energy absorbed by two layers at radius r [...] will be distributed evenly over the velocity interval $(v_{\min}, v)$ ..."

by using our notation. Scarlata states the same in (Scarlata and Panagia, 2015) on page 3.
Lets look at this quote in more detail:
The "energy absorbed at $w = z$ is $\sim 2\pi r \mathrm{d}z\mathrm{d}r$" (LW2021) (see figure 4.4 or in figure 4.3 it describes a small vertical strip respectively a small ring segment of the grey dashed end cap).
$\Rightarrow$ This is correct.

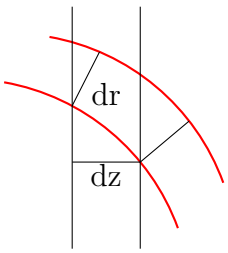

Figure 4.4: Segment, which absorbs a fraction of energy at $w = z$.

The "energy absorbed by the full shell segment is given by $r = w$ and $-1 \leq \xi \leq +1$ is $\sim 2\pi r(r - r_{\min})\mathrm{d}r = 2\pi rh\mathrm{d}r$" (LW2021) (grey dashed end cap in figure 4.3).
$\Rightarrow$ This is also correct.
"The ration of the absorbed energy at $w = z$ to the absorbed energy of the entire shell segment is

$$\frac{2\pi r\mathrm{d}z}{2\pi rh} = \frac{\mathrm{d}z}{h} \tag{4.41}$$

and in the integral

$$\int_{w}^{\sqrt{1+w^2}} \left(1 - e^{-\tau}\right) \frac{\mathrm{d}w}{h}\mathrm{d}v \tag{4.42}$$

with $\mathrm{d}w = \mathrm{d}z$ for $\gamma = 1$, which would give us the Scuderi integral for $\mathrm{d}w = \mathrm{const}$" (LW2021).
However, we want want to calculate the transmitted energy in the calculation of the absorption component. Therefore the wrong ratio is taken into account. Instead of equation 4.41, we have to use the energy at the projected velocity w scaled to the galaxy disc πr_0^2. "So instead of the ratio

$$\frac{2\pi r\mathrm{d}z}{2\pi rh} \tag{4.43}$$

we have to compute

$$\frac{2\pi r\mathrm{d}z}{\pi r_0^2} \tag{4.44}$$

[which] is the fraction of light taken out by a ring of radius r and width $\mathrm{d}z$, [...] which leads to our correct formula" (LW2021).

4.6 Non scaling-free case of the velocity integration approach

Now the calculations for the correct formula are done in the non scaling-free case, so that r_0 and v_0 remain. The velocity-radius relations stays

$$\frac{v}{v_0} = \frac{r}{r_0}. \tag{4.45}$$

The observed velocity is described by

$$v_{\mathrm{obs}} = v \cdot \cos(\theta) = v\frac{z}{r} = \frac{v_0}{r_0}z. \tag{4.46}$$

In the spatial approach nothing changes in the non scaling-free case. For the velocity approach, we have to transform the variables by

$$v = \frac{v_0}{r_0} r = \frac{v_0}{r_0}\sqrt{\xi^2 + z^2} = \frac{v_0}{r_0}\sqrt{\xi^2 + r_0^2 w^2}. \tag{4.47}$$

For a certain and fixed value of w it leads to

$$\frac{\mathrm{d}v}{\mathrm{d}\xi} = \frac{v_0}{r_0}\frac{\frac{1}{2}2\xi}{\sqrt{\xi^2 + r_0^2 w^2}} = \frac{v_0^2}{r_0^2}\frac{\xi}{v}, \tag{4.48}$$

which results in

$$\mathrm{d}\xi = \frac{r_0^2}{v_0^2} \cdot \frac{v}{\xi} \cdot \mathrm{d}v. \tag{4.49}$$

As lower integral limit we get $v(\xi = 0) = v_0 w$ and as upper integral limit $v(\xi = 1) = v_1 = \frac{v_0}{r_0}\sqrt{1 + r_0^2 w^2}$. The absorbed spectrum results in

$$F_{\text{absorbed}}(w) = \frac{L_w}{4\pi d^2}\frac{1}{r_0^2}\int_0^1 \left(1 - e^{-\tau(w,\xi)}\right) \cdot 2\xi \mathrm{d}\xi \tag{4.50}$$

$$= \frac{L_w}{4\pi d^2}\frac{1}{r_0^2}\int_{v_0 w}^{\frac{v_0}{r_0}\sqrt{1+r_0^2 w^2}} \left(1 - e^{-\tau(w,\xi)}\right) \cdot 2\xi \frac{r_0^2}{v_0^2}\frac{v}{\xi}\mathrm{d}v \tag{4.51}$$

$$= \frac{L_w}{4\pi d^2}\frac{1}{r_0^2}\int_{v_0 w}^{\frac{v_0}{r_0}\sqrt{1+r_0^2 w^2}} \left(1 - e^{-\tau(w,\xi)}\right) \cdot 2\frac{r_0^2}{v_0^2} v \mathrm{d}v. \tag{4.52}$$

We can test the calculation for the case $\tau \approx \infty$ and get

$$F_{\text{absorbed}}(w) = \frac{L_w}{4\pi d^2}\frac{1}{r_0^2} \cdot \left[\frac{r_0^2}{v_0^2} v^2\right]_{v_0 w}^{\frac{v_0}{r_0}\sqrt{1+r_0^2 w^2}} \tag{4.53}$$

$$= \frac{L_w}{4\pi d^2}\frac{1}{r_0^2}\frac{r_0^2}{v_0^2}\left(\frac{v_0^2}{r_0^2}\left(1 + r_0^2 w^2\right) - v_0^2 w^2\right) \tag{4.54}$$

$$= \frac{L_w}{4\pi d^2}\frac{1}{r_0^2} \tag{4.55}$$

which is results in the same result and interpretation as in section 4.2.

4.7 Absorption component in the case of a variable γ

In this section we discuss the calculation in the absorption case of a velocity law

$$\frac{v}{v_0} = \left(\frac{r}{r_0}\right)^{\gamma} \tag{4.56}$$

for the case of a variable γ and a non scaling-free case. The observed velocity is calculated by

$$v_{\text{obs}} = v \cdot \cos(\theta) = v\frac{z}{r} = v\frac{z}{\left(\frac{v}{v_0}\right)^{\frac{1}{\gamma}} r_0} = v_0^{\frac{1}{\gamma}} v^{1-\frac{1}{\gamma}} \frac{z}{r_0} \tag{4.57}$$

in dependence on v and is calculated by

$$v_{\text{obs}} = v\frac{z}{r} = v_0 \frac{r^{\gamma-1}}{r_0^{\gamma}} z \tag{4.58}$$

in dependence on r. The normed observed velocity is described by

$$w = \frac{v_{\text{obs}}}{v_0} = \frac{r^{\gamma-1}}{r_0^{\gamma}} z. \tag{4.59}$$

The fraction of cover of the radiation source (our galaxy) by an annulus by

$$\frac{2\pi\xi\Delta\xi}{\pi r_0^2} \tag{4.60}$$

remains the same as introduced in section 4.2. Therefore, we can calculate the absorption via the integral

$$F_{\text{absorbed}}(w) = \frac{L_w}{4\pi d^2}\frac{1}{r_0^2}\int_0^1 \left(1 - e^{-\tau(r)}\right) \cdot 2\xi \mathrm{d}\xi. \tag{4.61}$$

As the velocity is described by

$$v = v_0 \left(\frac{r}{r_0}\right)^{\gamma} = \frac{v_0}{r_0^{\gamma}} \left(\xi^2 + z^2\right)^{\frac{\gamma}{2}} = \frac{v_0}{r_0^{\gamma}} \left(\xi^2 + \left(w\frac{r_0^{\gamma}}{r^{\gamma-1}}\right)^2\right)^{\frac{\gamma}{2}} \tag{4.62}$$

the lower integral limit in the velocity space becomes

$$v\left(\xi = 0\right) = \frac{v_0}{r_0^{\gamma}} \left(w\frac{r_0^{\gamma}}{r^{\gamma-1}}\right)^{\gamma} \tag{4.63}$$

and the upper integral limit is

$$v\left(\xi = 1\right) = \frac{v_0}{r_0^{\gamma}} \left(1 + \left(w\frac{r_0^{\gamma}}{r^{\gamma-1}}\right)^2\right)^{\frac{\gamma}{2}}. \tag{4.64}$$

The spatial derivative of the velocity is calculated to be

$$\frac{\mathrm{d}v}{\mathrm{d}\xi} = \frac{v_0}{r_0^\gamma}\frac{\gamma}{2}2\xi\left(\xi^2+z^2\right)^{\frac{\gamma}{2}-1} \tag{4.65}$$

$$= \frac{v_0}{r_0^\gamma}\frac{\gamma}{2}2\xi\left(\frac{v}{v_0}r_0^\gamma\right)^{1-\frac{2}{\gamma}} \tag{4.66}$$

$$= \frac{v_0}{r_0^\gamma}\gamma\xi\left(\frac{v}{v_0}r_0^\gamma\right)^{1-\frac{2}{\gamma}} \tag{4.67}$$

$$= v_0 r_0^{-\gamma}\gamma\xi v^{1-\frac{2}{\gamma}} v_0^{\frac{2}{\gamma}-1} r_0^{\gamma-2} \tag{4.68}$$

$$= \frac{v_0^{\frac{2}{\gamma}}}{r_0^2}\gamma\xi v^{1-\frac{2}{\gamma}}. \tag{4.69}$$

We get

$$\mathrm{d}\xi = \frac{r_0^2}{v_0^{\frac{2}{\gamma}}}\frac{1}{\gamma\xi}\frac{1}{v^{1-2\gamma}}\mathrm{d}v \tag{4.70}$$

for the transformation of the integral from position to velocity space. The absorption component can be calculated by

$$F^\gamma_{\text{absorbed}}(w) = \frac{L_w}{4\pi d^2}\frac{1}{r_0}\int_0^1 \left(1-e^{-\tau(r)}\right)2\xi\mathrm{d}\xi \tag{4.71}$$

$$= \frac{L_w}{4\pi d^2}\frac{1}{r_0}\int_{\frac{v_0}{r_0^\gamma}\left(w\frac{r_0^\gamma}{r^{\gamma-1}}\right)^\gamma}^{\frac{v_0}{r_0^\gamma}\sqrt{1+\left(w\frac{r_0^\gamma}{r^{\gamma-1}}\right)^2}^\gamma} \left(1-e^{-\tau(r)}\right)2\xi\frac{r_0^2}{v_0^{\frac{2}{\gamma}}}\frac{1}{\gamma\xi}\frac{1}{v^{1-2\gamma}}\mathrm{d}v \tag{4.72}$$

$$= \frac{L_w}{4\pi d^2}\frac{1}{r_0}\int_{\frac{v_0}{r_0^\gamma}\left(w\frac{r_0^\gamma}{r^{\gamma-1}}\right)^\gamma}^{\frac{v_0}{r_0^\gamma}\sqrt{1+\left(w\frac{r_0^\gamma}{r^{\gamma-1}}\right)^2}^\gamma} \left(1-e^{-\tau(r)}\right)2\frac{r_0^2}{v_0^{\frac{2}{\gamma}}}\frac{1}{\gamma}\frac{1}{v^{1-2\gamma}}\mathrm{d}v, \tag{4.73}$$

where the optical depth is described by

$$\tau(r) = \tau_0\left(\frac{r_0}{r}\right)^{2\gamma+1} \tag{4.74}$$

with

$$\tau_0 = \frac{\pi e^2}{mc}f_{lu}\lambda_{lu}n_0\frac{r_0}{v_0}. \tag{4.75}$$

Chapter 5

Conclusion

Galactically scaled outflows are extremely important on many aspects and processes of galaxy evolution. They have impact on the loss of metals in galaxies and enrich the IGM with metals. Also, they remove gas, which would be available for star formation and transform the CGM. However, there are still many open questions regarding galactic winds and the comparison between theory and observations is far from clear.

After looking in detail on the SALT model for different parameter sets, a method to calculate 3D datacubes of galaxies with outflows is presented. From these datacubes, spatially resolved spectra can be extracted.

The outflow model on galactic scales by Scarlata 2015 is reimplemented. The SALT model uses the formalism introduced in stellar wind models and puts it on galactic scales. The outflow is assumed as a resonant radiatively driven wind and the spectrum shows a typical P-Cygni line profile. The P-Cygni profile consists of a blueshifted absorption component and an emission component. Spatial resolution is presented for different sizes of circular apertures. For a larger aperture size, the emission component increases and the absorption component gets filled. A library of spectra is computed for different parameter inputs to the model.

The SALT model is transferred to calculate 3D datacubes of galaxies with spherical outflows. These are 2D spatially and 1D spectrally resolved and the calculations are done numerically, a typical P-Cygni line profile appears for the outflow. By selecting a certain area of the galaxy, the spectrum can be calculated for this area. A spatially resolved spectral analysis of the outflow is presented for circular and quadratic apertures. However, with our method, every other geometry is possible.

The spectra of the datacube obtained by direct, numerical calculation are compared with the SALT model spectra. A difference in the absorption component occurred. The SALT model uses the ratio of the absorbed energy of a certain observed velocity to the absorbed energy of the total shell segment, for scaling the absorption component. However, the absorbed energy at a certain observed velocity compared to the galaxy disk has to be calculated, because in the absorption component the fraction, which is taken out of the continuum, is considered. This is implemented in the datacube. This difference has to be discussed with other groups working with the SALT model.

The spectra gained by the datacube are prepared to get compared to the MUSE measured data. A convolution on the numerically calculated data is applied. In spatial dimension a 2D Moffat profile is applied in the Fourier domain as the point spread function. Afterwards, in spectral, a 1D Gaussian kernel as line spread function is convolved with the data. After the convolution, the calculated spectrum can be compared with measured data.

The spectrum of the galaxy UDF884 is shown. This galaxy has a spherical outflow and the datacube was measured by MUSE. By looking on the MgII doublet line, the line resembles the course of a P-Cygni profile. Also in the spectra for different aperture sizes, the emission component increases for larger aperture sizes and the absorption component gets filled. This trend fits with the predictions from our datacube model.

Further work will be invested in fitting the datacube model on the measured data to determine different properties of the wind. A parameter discussion is presented. Probably three parameters of the six variable parameter in the model can be set on a fixed value for the fitting process of the model on real data. Therefore, less computational power will be needed to fit the model on data. The detailed analysis of the spatially resolved spectra of galaxies with spherical outflow geometries will be done on many samples. The introduced 3D datacube model for predictions of spatially resolved spectra of galactic outflows enables to do spatially resolved analysis of the measured data. With our datacube method it is possible to exploit the full potential of the data, measured by MUSE. The datacube model allows to study galaxy evolution by galactic winds.

Besides the important research of analysing outflow spectra and after fitting the model on data, an additional further step is to extend the existing datacube model, for example non-spherical outflows or multiple scattering.

Bibliography

R. Bacon, M. Accardo, L. Adjali, H. Anwand, S. Bauer, I. Biswas, J. Blaizot, D. Boudon, S. Brau-Nogue, J. Brinchmann, P. Caillier, L. Capoani, C. M. Carollo, T. Contini, P. Couderc, E. Daguisé, S. Deiries, B. Delabre, S. Dreizler, J. Dubois, M. Dupieux, C. Dupuy, E. Emsellem, T. Fechner, A. Fleischmann, M. François, G. Gallou, T. Gharsa, A. Glindemann, D. Gojak, B. Guiderdoni, G. Hansali, T. Hahn, A. Jarno, A. Kelz, C. Koehler, J. Kosmalski, F. Laurent, M. Le Floch, S. J. Lilly, J.-L. Lizon, M. Loupias, A. Manescau, C. Monstein, H. Nicklas, J.-C. Olaya, L. Pares, L. Pasquini, A. Pécontal-Rousset, R. Pelló, C. Petit, E. Popow, R. Reiss, A. Remillieux, E. Renault, M. Roth, G. Rupprecht, D. Serre, J. Schaye, G. Soucail, M. Steinmetz, O. Streicher, R. Stuik, H. Valentin, J. Vernet, P. Weilbacher, L. Wisotzki, and N. Yerle. The muse second-generation vlt instrument. In Ian S. McLean, Suzanne K. Ramsay, and Hideki Takami, editors, *Ground-based and Airborne Instrumentation for Astronomy III*, SPIE Proceedings, page 773508. SPIE, 2010. doi: 10.1117/12.856027.

E. Margaret Burbidge, G. R. Burbidge, and Vera C. Rubin. A study of the velocity field in m82 and its bearing on explosive phenomena in that galaxy. *The Astrophysical Journal*, 140:942, 1964. ISSN 0004-637X. doi: 10.1086/147997.

Cody Carr, Claudia Scarlata, Nino Panagia, and Alaina Henry. A semi-analytical line transfer (salt) model. ii: The effects of a bi-conical geometry. *The Astrophysical Journal*, 860(2):143, 2018. ISSN 0004-637X. doi: 10.3847/1538-4357/aac48e.

Cody Carr, Claudia Scarlata, Alaina Henry, and Nino Panagia. The effects of biconical outflows on ly a escape from green peas. *The Astrophysical Journal*, 906(2):104, 2021. ISSN 0004-637X. doi: 10.3847/1538-4357/abc7c3.

J. I. Castor, D. C. Abbott, and R. I. Klein. Radiation-driven winds in of stars. *The Astrophysical Journal*, 195:157, 1975. ISSN 0004-637X. doi: 10.1086/153315.

M. Eidelsberg, F. Crifo-Magnant, and C. J. Zeippen. Forbidden lines in hot astronomical sources. *Astronomy and Astrophysics Supplement*, (Vol. 43, P. 455), 1981.

Rob Garner. Messier 82 (the cigar galaxy). *NASA*, 06.10.2017. URL https://www.nasa.gov/feature/goddard/2017/messier-82-the-cigar-galaxy.

V. P. Grinin. Sobolev's approximation. *Astrophysics*, 44(3):402–410, 2001. ISSN 05717256. doi: 10.1023/A:1012884231706.

Timothy M. Heckman and Todd A. Thompson. Galactic winds and the role played by massive stars, 2017. URL https://arxiv.org/pdf/1701.09062.

Francois Henault, Roland Bacon, Christophe Bonneville, Didier Boudon, Roger L. Davies, Pierre Ferruit, Gerard F. Gilmore, Oliver LeFevre, Jean-Pierre Lemonnier, Simon Lilly, Simon L. Morris, Eric Prieto, Matthias Steinmetz, and P. Tim de Zeeuw. Muse: a second-generation integral-field spectrograph for the vlt. In Masanori Iye and Alan F. M. Moorwood, editors, *Instrument Design and Performance for Optical/Infrared Ground-based Telescopes*, SPIE Proceedings, page 1096. SPIE, 2002. doi: 10.1117/12.462334.

G. Israelian and M. de Groot. P cygni: An extraordinary luminous blue variable. *Space Science Reviews*, 90(3/4):493–522, 1999. ISSN 00386308. doi: 10.1023/A:1005223314464.

S. R. Kulkarni. Ay 126: Selection effects & forbidden lines. 2020. URL https://sites.astro.caltech.edu/~srk/Ay126/Lectures/Lecture6/Allowed_Forbidden.pdf.

Henny J. G. L. M. Lamers and Joseph P. Cassinelli. *Introduction to stellar winds*. Cambridge Univ. Press, Cambridge, 1. publ edition, 1999. ISBN 0521593980.

Henny J. G. L. M. Lamers and Emily M. Levesque. *Understanding stellar evolution*. AAS-IOP astronomy. IOP Publishing, Bristol, version: 20171201 edition, 2017. ISBN 978-0-7503-1278-3. doi: 10.1088/978-0-7503-1278-3. URL http://iopscience.iop.org/book/978-0-7503-1278-3.

C. R. Lynds and A. R. Sandage. Evidence for an explosion in the center of the galaxy m82. *The Astrophysical Journal*, 137:1005, 1963. ISSN 0004-637X. doi: 10.1086/147579.

Beena Meena, D. Michael Crenshaw, Henrique R. Schmitt, Mitchell Revalski, Travis C. Fischer, Garrett E. Polack, Steven B. Kraemer, and Dzhuliya Dashtamirova. Radiative driving of the agn outflows in the narrow-line seyfert 1 galaxy ngc 4051, 2021. URL http://arxiv.org/pdf/2103.12081v1.

J. H. Oort and G. W. Rougoor. The interstellar gas in the central part of the galaxy. *The Astronomical Journal*, 64:130, 1959. ISSN 00046256. doi: 10.1086/107903.

Donald E. Osterbrock. Interstellar matter in elliptical galaxies. ii. *The Astrophysical Journal*, 132:325, 1960. ISSN 0004-637X. doi: 10.1086/146930.

Simon Pasternack. Transition probabilities of forbidden lines. *The Astrophysical Journal*, 92:129, 1940. ISSN 0004-637X. doi: 10.1086/144208.

Joachim Puls, Jorick S. Vink, and Francisco Najarro. Mass loss from hot massive stars. *The Astronomy and Astrophysics Review*, 16(3-4):209–325, 2008. ISSN 0935-4956. doi: 10.1007/s00159-008-0015-8.

Keith Robinson. The p cygni profile and friends. In Keith Robinson, editor, *Spectroscopy*, Patrick Moore's practical astronomy series, pages 119–125. Springer, London, 2007. ISBN 978-0-387-36786-6. doi: 10.1007/978-0-387-68288-4{\textunderscore}10.

David Rupke. A review of recent observations of galactic winds driven by star formation. *Galaxies*, 6(4):138, 2018. doi: 10.3390/galaxies6040138.

C. Scarlata and N. Panagia. A semi-analytical line transfer (salt) model to interpret the spectra of galaxy outflows. *The Astrophysical Journal*, 801 (1):43, 2015. ISSN 0004-637X. doi: 10.1088/0004-637X/801/1/43. URL http://arxiv.org/pdf/1501.07282v1.

S. Scuderi, G. Bonanno, D. Spadaro, N. Panagia, H. J. G. L. M. Lamers, and A. de Koter. Properties and variability of the stellar wind from p cygni. *The Astrophysical Journal*, 437:465, 1994. ISSN 0004-637X. doi: 10.1086/175010.

Theodore P. Snow, Henny J. G. L. M. Lamers, Douglas M. Lindholm, and Andrew P. Odell. An atlas of ultraviolet p cygni profiles. *The Astrophysical Journal Supplement Series*, 95:163, 1994. ISSN 0067-0049. doi: 10.1086/192099.

V. V. Sobolev. *Moving Envelopes of Stars*. Harvard Books on Astronomy. Harvard University Press, s.l., 1960. ISBN 0674864638. doi: 10.4159/

harvard.9780674864658. URL http://www.degruyter.com/search?f_0=isbnissn&q_0=9780674864658&searchTitles=true.

Sylvain Veilleux, Gerald Cecil, and Joss Bland-Hawthorn. Galactic winds. *Annual Review of Astronomy and Astrophysics*, 43(1):769–826, 2005. ISSN 0066-4146. doi: 10.1146/annurev.astro.43.072103.150610.

Dong Zhang. A review of the theory of galactic winds driven by stellar feedback. *Galaxies*, 6(4):114, 2018. doi: 10.3390/galaxies6040114.

Selbständigkeitserklärung

Ich versichere,

- dass ich die Arbeit selbständig verfasst hat,
- dass ich keine anderen als die angegebenen Quellen benutzt und alle wörtlich oder sinngemäß aus anderen Werken übernommenen Aussagen als solche gekennzeichnet hat,
- dass die eingereichte Arbeit weder vollständig noch in wesentlichen Teilen Gegenstand eines anderen Prüfungsverfahrens gewesen ist,
- und dass das elektronische Exemplar mit den anderen Exemplaren übereinstimmt.

Stuttgart, den 09. April 2021 Anna Lena Schaible